MODELING THE DISCHARGE LOADING OF RADIO FREQUENCY EXCITED CO$_2$ SLAB LASERS

A Thesis submitted to the Faculty of

WORCESTER POLYTECHNIC INSTITUTE

in partial fulfillment of the requirements for the degree of

Master of Science

in

Electrical and Computer Engineering

By

_____

Saad Ahmad

(sahmad@wpi.edu)

September 07th 2011

APPROVED:

_____   _____

Prof. Reinhold Ludwig, Thesis Advisor   Prof. Sergey Makarov, Thesis Committee

_____

Prof. Fred Looft, Department Head

Abstract

RF excited CO_2 lasers are widely used in industry. They provide relatively high power discharge levels while maintaining compactness, simplicity, and durability with respect to other competing laser technologies. To attain high power levels in the range of 5-10 KW, lasers with large electrode areas have to be designed. Unfortunately, due to the large electrode length requirements, transmission line effects make the discharge loading nonlinear, adversely affecting the efficiency of the CO_2 laser. A standard approach to linearize the discharge loading is to introduce shunt inductors across the length of the electrodes in an effort to counter the capacitive nature of the discharge behavior.

This thesis investigates and improves the theoretical models found in the literature in an effort to predict the discharge non-uniformity and allow for multiple shunt inductors installation. Specifically, we discuss the coupling of a CO_2 laser discharge model with an electrical circuit solving scheme and how it can be characterized as one dimensional (1-D) and two dimensional (2-D) systems. The 1-D system is modeled using transmission line (TL) theory, where as the 2-D system is modeled using a finite difference time domain (FDTD) scheme. All our models were implemented in standard MATLAB code and the results are compared with those found in the literature with the goal to analyze and ascertain model limitations.

Preface and Acknowledgement

This thesis would not have been possible without the constant encouragement of all my professors at WPI and hence I would like to take this opportunity to thank them for being a source of encouragement and inspiration. I would like to specially thank Professor Ludwig, who was also my undergraduate Major Qualifying Project advisor and was always supportive and highly encouraging of all my endeavors. I would like to also thank Professor Alexander Emanuel and Professor Sergey Makarov, for being a source of inspiration and for having a great sense of enthusiasm for the sciences. I also thank my ex-roommates Kashif Azeem and Umair Khan for being great roommates and for making delicious tea. And lastly I thank my family and my wife Sara for being there and hearing me worry about my academic endeavors.

Table of Contents

Table of Figures

1   Introduction

A CO_2 laser is a molecular gas laser developed by *Kumar Patel* at Bell Labs in 1964 [1]. CO_2 laser uses the energy difference between the vibration levels of the ground state of CO_2 molecules to produce an infrared discharge centered at a wavelength of 9.6um or 10.6um[1]. The focus of this thesis will be on CO_2 lasers, which are RF-excited and are in a slab configuration. Such a laser is typically constructed using two parallel electrodes in one dimension, ceramic spacers in the second and mirrors in the third as is shown in Figure 1. The resulting rectangular volume contains the laser gas mixture, which is excited by an RF source connected between the two electrodes. The resulting laser light is then reflected back and forth in the resonant cavity which is constructed by having high reflectivity mirrors along the laser length. These lasers are at the forefront of the CO_2 laser technology due to their stability, durability and simplicity in comparison with other competing technologies [2]. *Abramski et al.* [3] demonstrated that the electrode area scales proportionally with the RF excited slab laser discharge power and ever since there has been a push towards increasing the electrode area to attain higher power discharge levels. The increase in electrode lengths results in non-linear gain media uniformity along the length of the laser if the length of the laser becomes a significant factor of the RF wavelength. The resulting voltage standing waves along the laser can be smoothed to improve the laser efficiency by connecting lumped inductors in shunt along the laser length to counter the capacitive discharge impedance as shown in Figure 1. This approach works best in narrow channel devices and there have been numerous papers in the literature which address the problem of nonlinear standing wave voltages across the laser length for narrow channel devices (see section 1.1 for more details). However, a similar approach can be used in wide channel waveguides while taking into account the effects of the discharge loading [4].
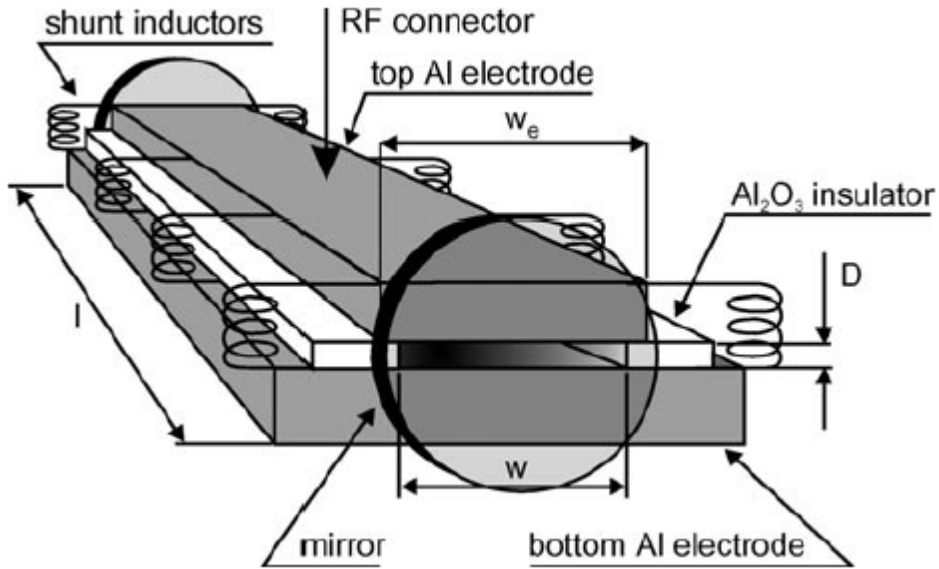
Figure 1: A typical CO_2 laser slab geometry, depicting relevant dimensions and important design features [5].

As mentioned previously, discharge power is dependent on the electrode slab area, and hence the length, or the width, of the resonant structure can be increased to increase the power loading. However, since increasing the length beyond a certain extent is impractical, increasing the electrode width becomes desirable in order to enhance the laser power discharge loading. The problem with this approach of increasing slab laser width is that as the width reaches 20% of the laser length, simple design models such as a 1-D analysis becomes inadequate, and a 2-D model becomes essential. The 2-D model allows the effects of the width-wise voltage variations to be observed. They also allow predicting the effect of the ceramic spacers which are placed along the length of the laser to maintain the electrode gap and the RF shielding of the laser system. Figure 2 shows a typical CO_2 slab laser geometry which has been adopted as a candidate for this essential 2-D model.
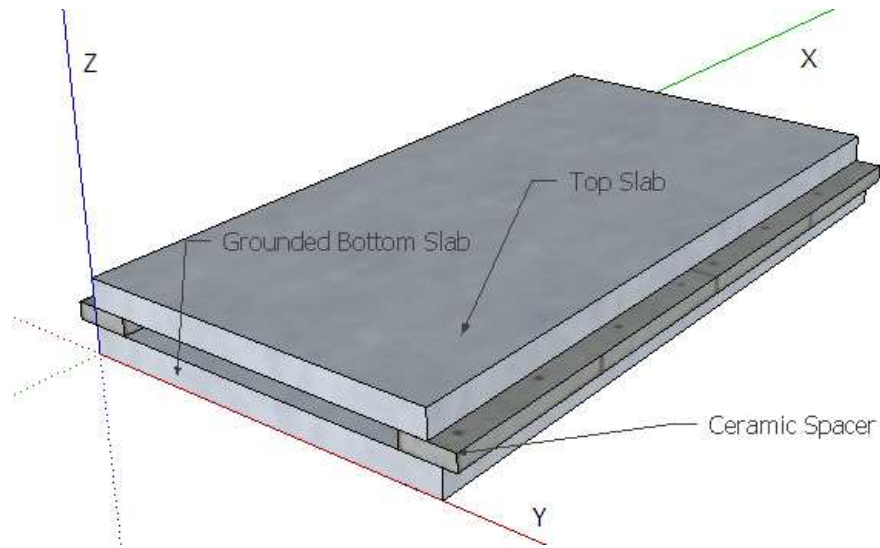
Figure 2: Slab Laser with the two electrodes and ceramic spacers shown.

Due to the non-linearity of the standing wave voltages, proper placement of shunt inductors is of vital importance and requires modeling of standing wave voltages. The first proposed narrow channel model for the purpose of simulating standing wave voltages along the laser length was proposed by *Lapucci et al.* in [4] and by *Strohschein et al.* in [2]. These 1-D models incorporated RF standing wave theory with the CO_2 discharge laser model and used the Telegrapher's equations to obtain the voltage amplitude profiles along the laser length. However a similar level of development for the 2-D model, which is important for wide channel waveguides, has not been observed. The first 2-D approach for this wide channel problem was put forth by *Spindler* [6] in 2003, in which a 2-D finite difference time domain (FDTD) algorithm incorporated Maxwell's equations with *Vitruk's* CO_2 laser discharge model [7] by using a 2-D Cartesian grid. This thesis work will research and investigate the various standing wave voltage models which are present in the literature and which will culminate in a 2-D FDTD model implementation. Theoretically, the 2-D model should be sufficient to model slab lasers of any aspect ratio, since for the lower aspect ratios the model predictions should converge to the 1-D TL models. Hence we will present the 2-D model as a design tool for determining the optimal

shunt inductor placement locations for a given slab laser geometry. More specifically, Chapter 2 presents CO_2 background and theory along with *Vitruk's* laser discharge model, Chapter 3 and 4 implement and explore the 1-D and 2-D models, and Chapter 5 concludes by defining the model limitations and discussing the boundary conditions, while proposing further areas of interest for model evolution.

1.1 Literature Research

As mentioned earlier, one of the first proposed 1-D approaches for modeling the voltage profiles along a narrow channel CO_2 laser length were proposed by *Lapucci et al.* in [4] and *Strohschein et al.* in [2]. Both these approaches used *Vitruk's* CO_2 laser discharge model presented in [7] where *Vitruk et al.* experimentally measured laser parameters and proposed modeling the discharge impedance as a combination of a lumped components. They divided the CO_2 laser discharge into two transversal regions, with a positive ionic region near the electrodes being modeled by a capacitor and a plasma region in the middle being modeled by a parallel combination of a capacitor and resistor. The discharge model is presented in more detail in Section 2.1.
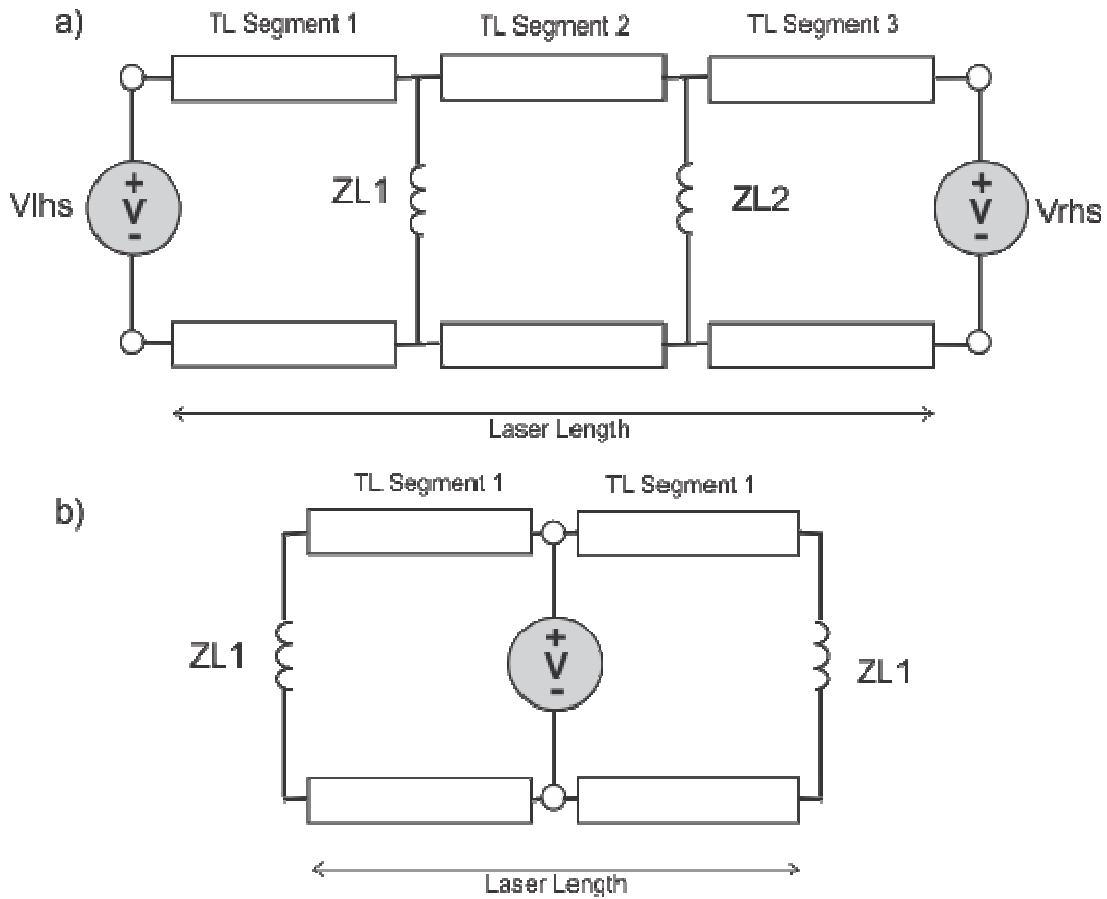
Figure 3: 1-D TL model configurations for CO_2 Laser, a) Side-driven RF sources configuration is assumed in [2] and in b) a centrally RF excitation is assumed in [4].

In [4], Lapucci et al. present a theoretical model for 1KW CO_2 slab laser. The model assumes a centrally fed laser which has a pair of termination inductors on either end to improve the discharge nonlinearity. The laser is modeled as two lossy transmission lines (TL) in parallel as the model is centrally fed by a RF source, with the TL propagation constant and characteristic impedance being determined by the type of laser discharge. The paper also presents experimental results for comparison with the simulation results, by using paper capacitors and chips resistors within the slab structure to represent the laser discharge impedance.

In [2], *Strohschein et al.* present a computational model for CO_2 slab lasers. This model is similar and more comprehensive than the one in [4] since it fully incorporates *Vitruk's* discharge formulation and allows multiple inductors to be installed at various locations along the laser length, and thereby breaks up the laser model into TL segments separated from each other by the shunt inductors. The model is presented for a laser which is side driven by two RF sources on either sides. A more detailed explanation of both 1-D models and their implementation is presented in Section 3.2.

In 2003, *Spindler* proposed a 2-D FDTD model which incorporates *Vitruk's* discharge model into a Transverse Magnetic (TM) FDTD simulation. The method used is similar to the ones seen in the 1-D models except that *Vitruk's* discharge model is incorporated by iteratively changing the permittivity and the conductivity values of each cell of the FDTD Cartesian grid. This approach allows easy incorporation of lumped components into any point along the laser geometry and also enables transient analysis of the voltage and power distribution across the laser slab. The paper, however, does not provide experimental validation of the model. A more detailed presentation of this model is made in Chapter 4 where we implement the model and compare the results with those reported in the literature.

2   Laser Background and Theory

Since the discovery of the photoelectric effect by Hertz in 1887, it was known that when light of a certain wavelength is shone on matter, it was possible to elevate electrons into higher energy states. However, it was not until 1917 when Einstein showed that the reverse, which he called stimulated emission, is also possible. He showed that it was possible to shine a photon on an already excited atom and cause the electron to jump to a lower energy state and emit a photon that was identical in direction, phase, polarization and frequency to the incident photon. This principle is pictorially depicted in Figure 4. The energy difference between the ground and excited stages of the atom given by Eq. (0), determines the required photon wavelength that is needed to initiate stimulated emission.
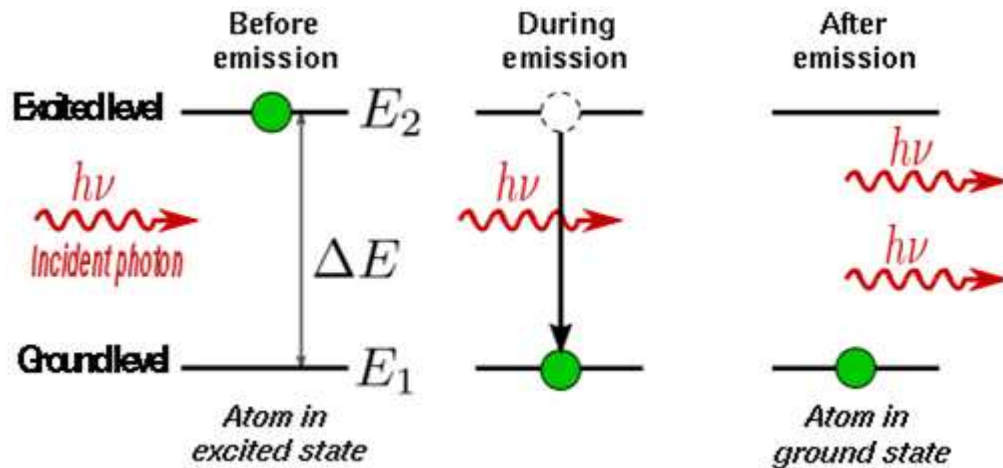
Figure 4: Stimulated emission - the difference between the energy level dictactes the frequency of the photon that is needed [8].

$$E_2 - E_1 = \Delta E = h\,v \tag{0}$$

Where, h is Planck's constant, and v is the photon's wavelength.

Lasers utilize stimulated emission theory in their operation and that is why the acronym LASER stands for light amplification by stimulated emission of radiation. However, under normal

conditions photon absorption exceeds stimulated emission, and hence for lasers to be possible, the so-called population inversion is needed; that is the majority of the electrons need to be excited to a higher energy state. Population inversion can be obtained by a process known as laser pumping in which electrical or light energy is pumped into the laser material. As laser pumping is initiated and population inversion achieved, a single emission of photon can cause stimulated emission, and hence an avalanche of identical photons. These photons are then reflected back and forth between silver coated high reflectivity mirrors along the resonant cavity. One of these mirrors is designed to be of slightly lower reflectivity to allow some of the photons to be emitted in the form of a laser discharge. As the laser discharge commences, some of the electrons drop to a lower energy state and hence laser pumping needs to be continued to move these electrons back to the higher energy stage in order to maintain the population inversion and hence the laser discharge.

The first working laser prototype was invented in 1960 by Ted Maiman [9]. This laser operated in the pulsed mode and was a solid state laser made out of synthetic ruby crystals, which are essentially aluminum oxide with chromium ion impurities. When the light is flashed on these crystals the electrons in the chromium ions are excited to higher energy states and the decay of these electrons to lower energy states resulted in a laser discharge with a wavelength of 594.3nm. The light was flashed intermittently, and this resulted in the pulsed laser operation. Since this first laser there have been a plethora of laser systems with applications in almost every field, ranging from telecommunications to medical surgery.

Lasers can be categorized by the types of active media they employ, and these media can be divided broadly into solid, liquid and gas. Figure 4 shows the wavelength ranges that these laser families fall in to and as can be seen the gaseous laser family is the most diverse family of lasers.
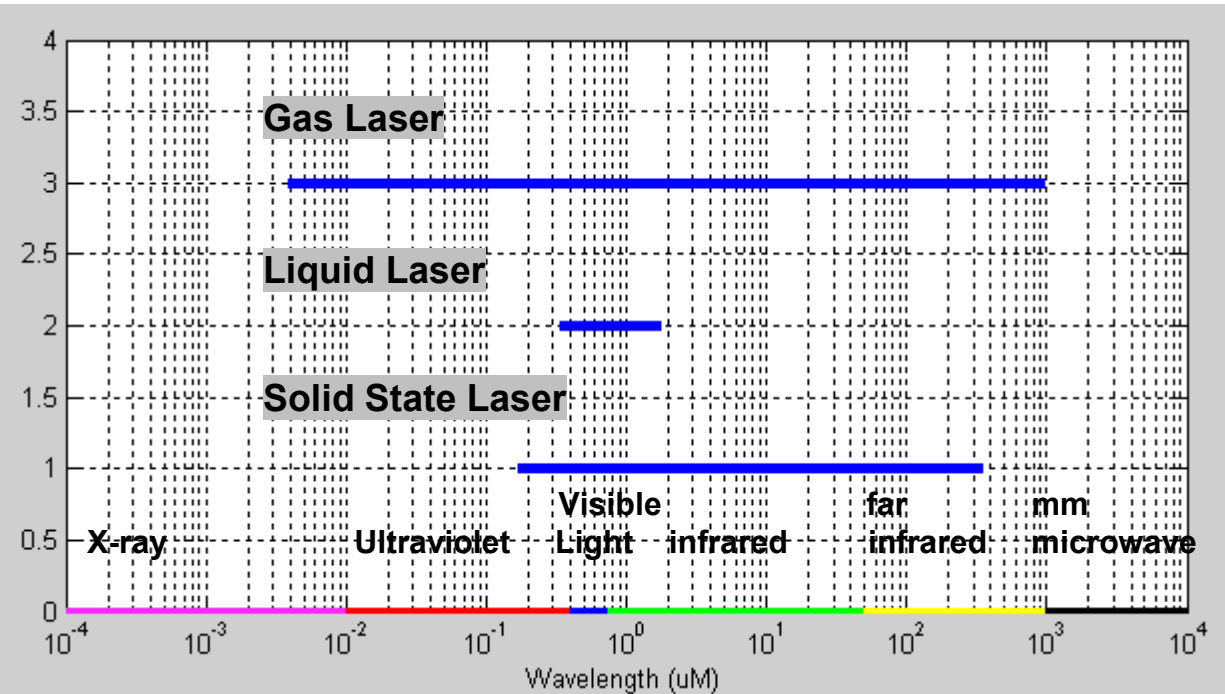
Figure 5: Reported ranges of output wavelengths for various laser media [10].

In the next sections we provide some background that is common among these laser families and highlight differences between them.

2.1 Solid State Lasers

Solid State (SS) lasers were the first type of laser to be invented and they have the advantage of being rugged and suitable for non-laboratory environments [9]. In general, SS lasers use crystalline gain media, like glass or ceramics. The gain media are doped with rare earth elements as their ions reach lasing thresholds at fairly low pumping energy levels and hence

neodymium and erbium are commonly used. Commonly semiconductor lasers are also included in this category as they are solid state devices even though their operation differs from a typical solid state laser. Although hundreds of media can be used to make solid-state lasers, only few are commonly used, like the neodymium-doped YAG, the neodymium-doped glass (Nd:glass), ytterbium doped glasses and ceramics which are used in extremely high power (terawatt scale) applications [11]. Solid state lasers are usually pumped using flash-lamps and arc-lamps as shown in Figure 6, which is a simplified diagram of a ruby laser.
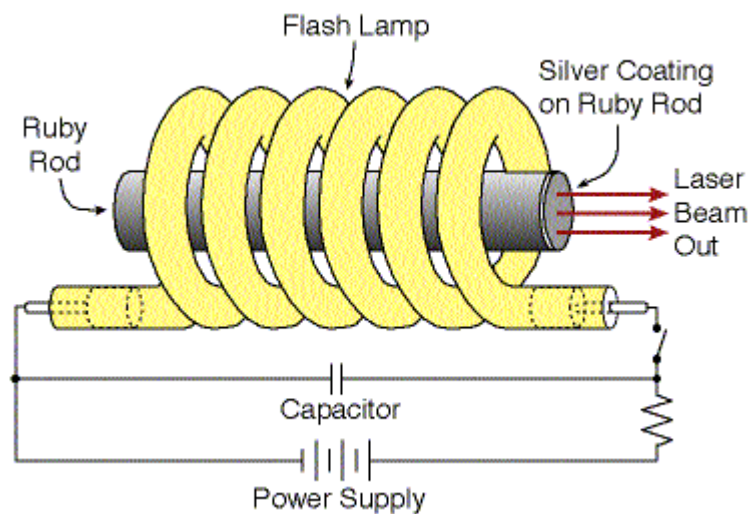
Figure 6: Solid state laser with a flashlamp pump [12].

Diode-pumped semiconductor device lasers tend to be more efficient because they are semiconductor lasers that can be electrically pumped and do not require the use of inefficient flash lamp pumping. SS and other lasers can be operated in the following modes:

- Continuous Wave (CW) – CW operation implies that the laser is being continuously pumped and emits light continuously.

- Quasi continuous wave (Q-CW) – Q-CW mode implies that the laser pump's duty cycle is sufficiently reduced to minimize the thermal stresses of the gain media significantly, but high enough to operate the laser in steady state i.e. the laser light seems to be a

continuous wave optically. This is desirable since for certain gain media CW operation results in heating up of the gain medium and in such cases Q-CW mode is preferred [13].

- Pulsed mode – Pulsed SS lasers usually use flash lamps, with the input power being determined by multiplying pulse energy in watts with the number of pulses per second.

SS lasers are used in a wide range of diverse applications, varying from welding, cutting, drilling, semiconductor fabrication, high-end printing, range-finding, to medical surgeries etc.

2.2 Liquid Lasers

Liquid lasers are also commonly known as dye lasers, as they commonly use organic dyes as the lasing or gain medium, even though solid state dye lasers are also available. Liquid laser are very versatile and use simpler technology when compared with other families of laser and hence can be put together by scientific labs when needed [15]. Liquid laser was discovered by *P. P. Sorokin* and *F. P. Schäfer et. al* independently in 1966. The organic dye is usually mixed with a solvent like ethanol or chloroform, and is contained in a cell that has a circulation connection with a larger container as the organic dye degrades due to the lasing process. Liquid laser's lasing thresholds are usually high and are typically achieved by optically pumping the laser medium by short pulses from a flash lamp. The liquid nature of the lasing medium allows for a more flexible architecture and hence a few different design configurations are found in literature for liquid lasers [14]. The broad gain spectra and emission range of liquid lasers result in systems with a typical bandwidth of approximately 50nm and hence makes them ideal

candidate for research applications from fundamental physics to clinical medicine. Some other applications are in photophysical, photochemical and spectroscopy applications [15].

A dye laser configuration for a coaxial flash lamp pumping is shown in Figure 7.
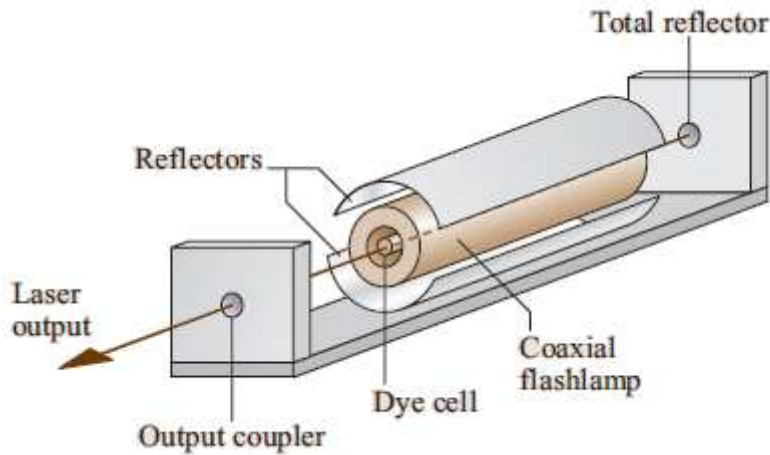
Figure 7: Coaxial flash lamp pumped dye laser [15].

2.3 Gas Lasers

In gas lasers the active medium is gaseous, and the lasing threshold is achieved by directly passing an electric current through the gas mixture. The first gas laser was of the He-Ne family and was invented by *A. Javan* and *W. R. Bennet* at Bell labs in 1960. The invention was of particular importance as it was the first laser to operate in the CW mode and was able to convert electrical energy into laser output energy [16].

Gas lasers are of particular importance as we saw earlier in Figure 5; these lasers have the largest spectral range of any laser family, ranging from extreme ultraviolet to sub mm range, and the largest power discharge output, ranging in 100s of KW for large CO_2 lasers. Gaseous

gain medium is also relatively cheap and allows easier heat transfer and hence relatively higher operating temperatures. Gas lasers can be divided into molecular, atomic and ionic gas families. The molecular laser can be further divided as per the type of stimulated emission used in the lasing transition i.e. electronic, vibration or rotational. These transitions determine the laser wavelength and the energy that is required to achieve lasing and the energy that will be lost as heat. For example, a N_2 molecular laser uses electronic transitions whereas the CO_2 molecular laser uses vibrational-rotational transitions [10].
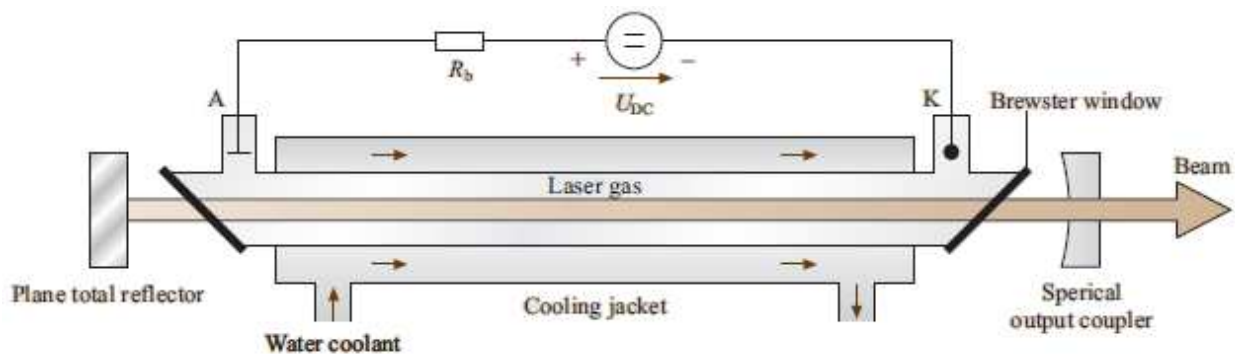
Figure 8: Longitudinally DC discharge gas laser configuration [15].

As mentioned earlier gaseous gain media have to be excited electrically, as gases have narrow absorption lines making optical pumping inefficient. The current can be passed as CW at RF frequency or through pulses or by using a DC voltage discharge. For both RF and DC operation the laser configuration utilizes two electrodes for electrical excitation with the gas mixture contained between them. A common configuration for gas lasers utilizes a longitudinal DC discharge and a circulating water cooling system, as is shown in Figure 8. It should be noted that this laser configuration does not require the gas mixture to be changed or circulated as it achieves heat transfer by using water circulation to cool the electrodes. During the laser discharge ions and free electrons acquire kinetic energy from the applied electric field and transfer this energy to neutral atoms through collisions. Electronic excitation is efficient for gases as there is no vibrational loss and in some cases another gas in addition to the gain

13

medium can be included which on being excited can transfer the energy through vibrations to the gas of interest [15].

2.4 CO$_2$ Laser

A CO$_2$ laser is a molecular gas laser originally developed by *Kumar Patel* at Bell Labs in 1964. CO$_2$ lasers use an active medium that consists of a gas mixture of CO$_2$, N$_2$ and He. CO$_2$ laser uses vibration levels of the CO$_2$ molecule, as the energy difference between these two levels results in an infrared discharge centered at 9.6um or 10.6um [1]. N$_2$ and He are used for increasing the laser efficiency. RF excited laser pumping uses an electric field which transfers energy to nitrogen molecules through collisions with the electrons, and since N$_2$ is homonuclear it does not lose this energy by emitting photons and is able to transfer this energy to CO$_2$ through collisions and this leads to the necessary CO$_2$ population inversion. N$_2$ after collisions with CO$_2$ is left in a lower energy stage, and further collisions with Helium transition it to the ground stage. As a result of these collisions the Helium molecules are heated and need to lose this heat to facilitate the population inversion process and they do so by colliding with the metal slabs and the ceramic spacers. In sealed off lasers where the gas mixture is not changed other gases are added in small amounts to prevent the disassociation processes which decrease the operational life of a CO$_2$ laser and commonly Hydrogen and Xenon are used as additives in CO$_2$ lasers [15]. Hence in short the gas mixture composition plays an important role in maintaining the lasing processes.

The maximum theoretical efficiency of a CO$_2$ laser, as ascertained from the energy level diagrams is 38%. However, no CO$_2$ laser comes close to this number and most CO$_2$ lasers are only 20% efficient. Like any gas laser the input power is provided by electrical means and the difference between the input electrical power and the laser discharge power is heat energy which needs to be lost. This 20% CO$_2$ laser efficiency means that 80% of the energy is lost as heat, which then needs to be transferred away and hence it is this method of heat removal which characterizes the type of CO$_2$ laser design for a given laser output power parameter. CO$_2$ lasers can be sealed-off systems, fast-flow high power systems and even pulsed systems. The

simplest method of heat removal is to use the thermal conductivity of the gas mixture for heat exchanges during collisions with the cooled walls of the container. For a given maximum gas mixture temperature rise ΔT, the maximum laser discharge power, P_{DIS} can be by calculated by solving the differential heat transfer equation for the given laser geometry. This method is usually used in CW systems and results in lasers of 100W or less. The second method is to remove the gas mixture itself for removal of heat energy and this method is usually called a fast-flow system and results in lasers which result in laser output in the KW range [15]. The amount of heat removal can be calculated by using the gas mixture's specific heat capacity and mass flow. The third method uses higher pressures for obtaining higher ΔT. The heat capacity of the gas mixture is around 300J per liter of gas at 1 atmosphere, and as input and output power is proportional to the gas density the gas mixture pressure can be increased to maximize the laser output power [17].

2.4.1   RF Excitation

Even though both DC and AC discharges are possible, RF excitation is widely used in CO_2 lasers. It allows higher gas mixture pressures and higher energy densities while maintaining a stable and uniform laser discharge and hence avoids degradation caused by the permanent cathode and anodes used for DC discharges.
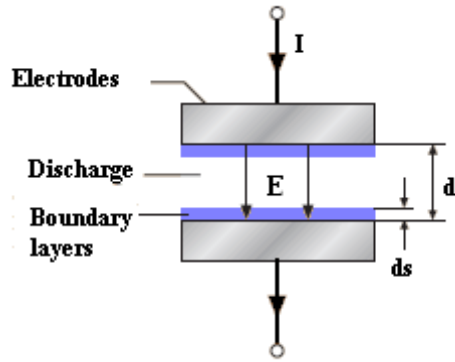
Figure 9: RF excitation using a slab laser configuration.

A common way of exciting a CO_2 laser is to use capacitively coupled transverse excitation where the upper electrode is excited while the bottom electrode is grounded, and this result in current flow from the top to the bottom electrode as is shown in Figure 9. As mentioned earlier, RF discharges can be both longitudinal and transversal. Transversal RF excitations are of greater interest to us, as they require lower voltages than for a longitudinal discharge due to the smaller size of the transverse separation between the bottom and the top slab. Hence for a longitudinal discharge much higher voltages need to be used for obtaining the same laser discharge power. Electric fields need to be sufficiently high to start and maintain the self-sustained laser glow discharge; in the transversal configuration around 100V per mm of the electrode gap is required, for a given gas mixture pressure. In certain CO_2 laser configurations the electrodes are insulated from the gas mixture in which case the current flow is just the displacement current given by the displacement current term of the Maxwell's equation. In this thesis research we model electrodes which are in direct contact with the active medium. This direct contact with the gas mixture results in ions being attracted to the two electrodes and hence the electron density near the electrodes is reduced.

The power loss in the ion sheaths reduces the laser efficiency. The ion sheath thickness is denoted, d_S, and is inversely proportional to the frequency of excitation. At 125 MHz the value

of d_S is approximately 0.35 mm (for a pressure of 9 kilopascals) and hence the value of d or electrode separation has to be larger than this value. However increasing the electrode gap, d adversely affects the heat dissipation in the laser. Usually a sweet spot is found at RF frequency of around 100 MHz and 2mm electrode separation. It should be noted that 100 MHz falls in the FM Radio frequency band hence the laser casing has to be properly shielded.

The behavior of discharge in a laser is very different from that of a simple resistor as depicted in Figure 10.
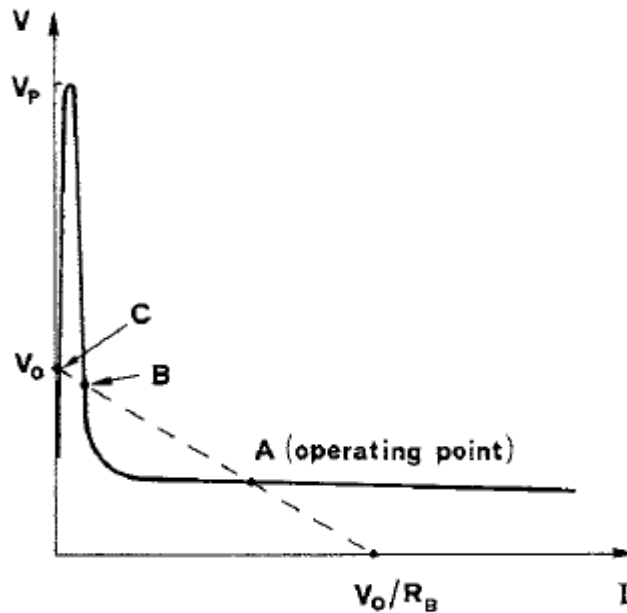
Figure 10: VI characteristics of the laser discharge and the voltage source with a series resistor [18].

The solid line represents the VI characteristics of the laser discharge, while the dotted line represents the VI characteristics of the voltage source with a series resistor called the ballast resistor (R_B) added. And as can be seen, point A represents the operating point of the laser at which the voltage is insensitive to the current fluctuations. It should be noted that the laser can obtain a stable equilibrium at points A and C, but not a B, which represents an unstable

equilibrium point. It also has to be noted that for the laser to operate at point A the voltage peak of V_P, which is much higher than the operating points, needs to be applied otherwise the voltage stabilizes at point C [18]. The value of the ballast resistor R_B also plays an important role as it moves the operating point A to the desired power discharge level by varying the discharge current.

2.4.2   CO$_2$ Laser Construction

The CO$_2$ slab laser is usually constructed as shown in Figure 1. The top metallic electrode is excited by an RF source and the bottom metallic electrode is grounded; the electrodes are maintained at their defined width by the ceramic spacers, which have relative dielectric permittivity of around 9.7 and low dielectric losses. Along the X-axis the cavity is enclosed by two mirrors that are usually made of copper and coated with gold or with dielectric layers; this makes for a highly reflective resonant cavity. One of these mirrors is of a lower reflectivity and hence allows the laser discharge output. This resulting enclosed rectangular cavity contains the gas mixture and hence for our models the gas mixture is contained in a rectangular volume given by the product of the laser width, length and the slab separation.

2.4.3   CO$_2$ Laser Discharge

The Alpha-Mode CO$_2$ laser discharge model being used in this project was proposed by *Vitruk et. al* [7], which formulated similarity and scaling laws for the discharge parameters as a function of the RF voltage and currents. The model uses experimental laser data to model the discharge using passive components. The experimental data was obtained over a frequency range of 100-160MHz, pressure range of 40-100torr and the inter-electrode gap range of 1-3mm and for a

He:N_2:CO_2 = 3:l:l + 5% Xenon gas mixture as these are the parameter ranges of a typical CO_2 laser.

The discharge model has input parameters of gas pressure p, excitation frequency f, electrode gap d, and the local current density J_D; they collectively determine the values of C_S, C_P and R_P shown in Figure 11. We next outline how this discharge model will be coupled into the 1-D TL models and the 2-D FDTD model.
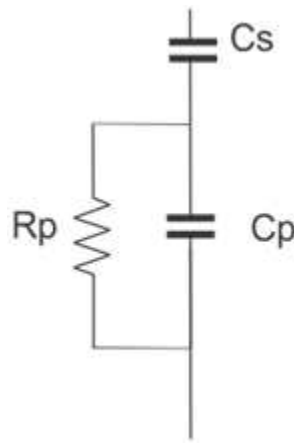
Figure 11: Alpha mode RF discharge model, valid for negligible sheet power dissipation.

The discharge model can be divided into two transversal sections, ion sheets adjacent to the electrode surface and a weakly ionized plasma column, which constitutes the active gain region. The plasma column oscillates at the RF excitation frequency as the positive ions are attracted to one or the other electrode depending on the electrode polarity, as shown in Figure 12.
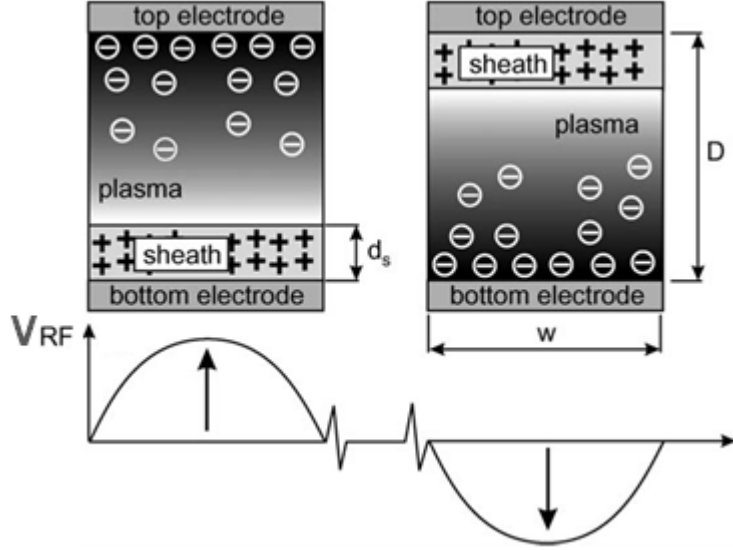
Figure 12: The ion sheath and the plasma column distribution dependence on V_{RF} polarity [5].

The less mobile positive ions appear closer to the electrodes where as the more mobile electrons are spread almost throughout the electrode gap, which is desirable as under optimal conditions the plasma column region would occupy most of the electrode gap. As the ion sheath is assumed to be non-conductive it is modeled by the Capacitor C_S and the conductive plasma column is modeled by a parallel combination of C_P and R_P.

$$C_S = e_0 \frac{S}{d_S} \tag{2}$$

$$C_P = e_0 \frac{S}{(d-d_S)} \tag{3}$$

$$R_P = \frac{V_P}{\sqrt{(J_d S)^2 - (w C_P V_P)^2}} \tag{4}$$

where S is the surface area of interest, d_S is the time averaged ion sheet thickness found using (5), and J_d is the local transversal current density and V_P the plasma column voltage given by (6).

$$d_S f = 42 \; mmMHz \tag{5}$$

$$V_P = \left(a + \frac{b}{p}\right) p(d - d_S) \tag{6}$$

where a = 156Vrms/(m.Torr) and b = 44Vrms.

It should be noted that the constants used in (5) and (6) have been derived from Vitruk's experimental results. However, later in [19], Baker came up with more accurate experimental results which revise the constant values: $d_S f$ = 58mmMHz, a = 378Vrms/(m.Torr) and b = 41.5Vrms. This meant that the dielectric constant value of the discharge was lower and the plasma voltage higher than previously anticipated. The result of this parametric improvement on V_P can be seen in Figure 13, especially at the higher gas mixture pressures.
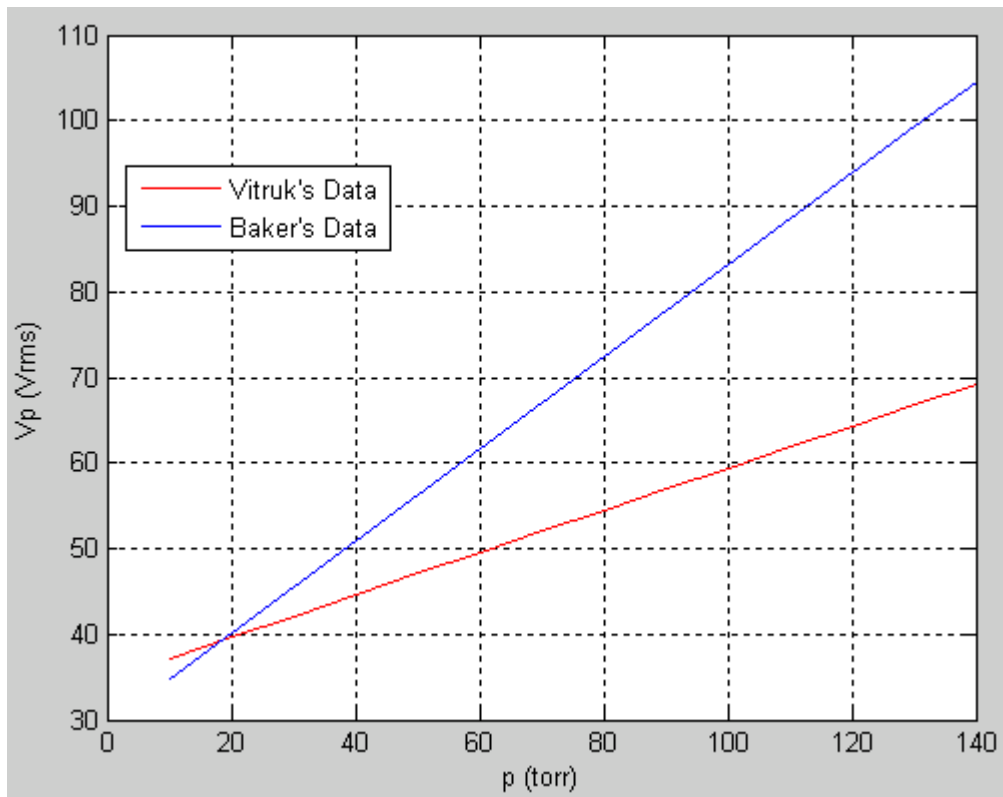
Figure 13: Vp versus the gas mixture pressure curves for Vitruk's and Baker's data.

Hence the overall discharge impedance Z_D, given by (7), is a parallel combination of plasma column resistance R_P and capacitance C_P given by (3) and (4) respectively, in series with the ion sheet capacitance C_S given by (2).

$$Z_D = R_D + iX_D \tag{7}$$

For the 1-D models the TL conductance G and TL capacitance C are found using (8) and (9), which assumes that the structural capacitance for the laser structure is much less than the discharge capacitance. If the laser being modeled is a large electrode area laser then we will have to account for the laser's structural capacitance in (9).

$$G = Real\left(\frac{1}{Z_D}\right) \tag{8}$$

$$C = Imag\left(\frac{1}{Z_D}\right) \times \frac{1}{2\pi f} \tag{9}$$

For the FDTD 2-D models the discharge model can be incorporated through the effective permittivity and conductivity terms given by (10) and (11), respectively.

$$\varepsilon_{eff} = \varepsilon_0 Imag\left(\frac{1}{Z_D}\right) \times \frac{d}{2\pi f \varepsilon_0 S} \tag{10}$$

$$\gamma_{eff} = Real\left(\frac{1}{Z_D}\right)\frac{d}{S} \tag{11}$$

2.4.4 Laser Discharge Impedance Behavior

Before moving forward to the laser model it is instructive to study the laser discharge impedance versus the power loading. It can be seen that for no power discharge the capacitive reactance tends towards 14Ωm and for the high power loading conditions it tends towards C_S.
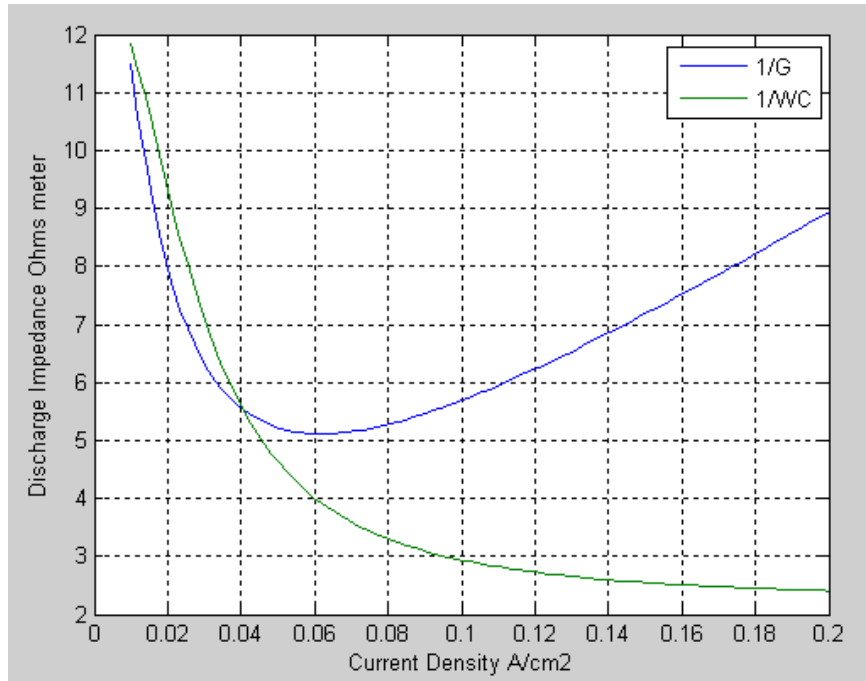
Figure 14: Discharge impedance versus current density behavior.

From Figure 15 it can be seen that the discharge power is proportional to J_D.
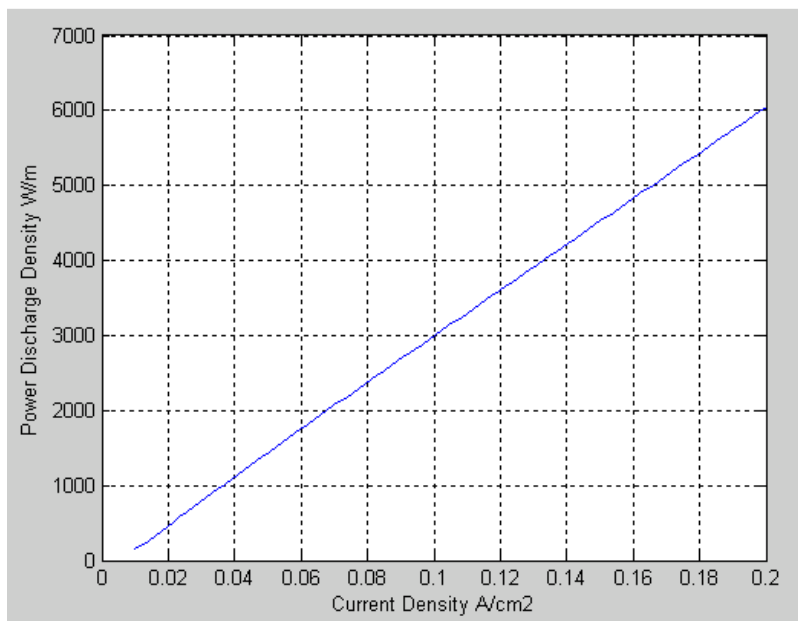
Figure 15: Power discharge density versus current density behavior.

24

2.5 Thesis Objectives

CO_2 lasers are the most powerful lasers in the world, and to increase the output power further larger electrode areas are needed. Even though the 1-D models have been present in the literature for some time, a more effective modeling approach is of interest. These 1-D and 2-D models allow the optimum placement of shunt inductors and thereby allow the maximization of laser output power. As mentioned earlier increasing the slab area by increasing the laser length beyond a certain degree is impractical and hence increasing the laser width becomes important. The effect of this increase in the aspect ratio results in increased importance of the 2-D laser models, as the 1-D models will not show the voltage variations along the laser width. With just the 1-D models, effects such as that of placing the shunt inductors at various points along the laser width and not just the laser length or the effect of the RF shielding of the laser on the voltage variations along the slab will be lost. Further, the FDTD modeling approach will allow the transients to be observed and also allow the incorporation of a more complex RF excitation source. Hence, the thesis objectives can be summarized in the following manner:

1. Study and implement any 1-D computational methods found in literature for predicting laser voltage distributions.

2. Study and implement the 2-D computational approach as advocated by Strohschein and compare the results with the 1-D model.

3. Evaluate the 2-D model and incorporate more advanced RF source models and investigate the effect of the ceramic spacers and RF shielding of the laser system.

4. Summarize differences between the 1-D and 2-D model and ascertain their boundaries.

5. Just like the 1-D model assumes that everything is uniform along the laser width and height, the 2-D model assumes that everything in a laser in the z-dimension is uniform. The need and a possible implementation of a 3-D approach will need to be discussed.

3   1-D CO$_2$ Slab Laser Algorithms

The focus of this chapter will be on 1-D models which are commonly utilized for laser design optimization and more specifically for obtaining shunt inductor placement co-ordinates. These models utilize TL theory and hence require a thorough understanding of TL concepts and a method for solving voltage and current wave equations for a system of multiple TL segments. We introduce one such method in the form of a steady state TL system solver algorithm in section 3.1 before incorporating it with Vitruk's CO$_2$ laser discharge model in section 3.2 & 3.3, and presenting our simulation results in section 3.4.

3.1   TL system solver

CO$_2$ lasers are modeled as a system of TLs with each slab segment being separated by a shunt inductor as shown in Figure 18. Hence for introducing the TL solver which can solve for voltage and current waves we assume a geometry shown in Figure 16. As shown, there are two TL segments, with specified propagation constant and characteristic impedance, and a thevenin voltage source and a specified load.
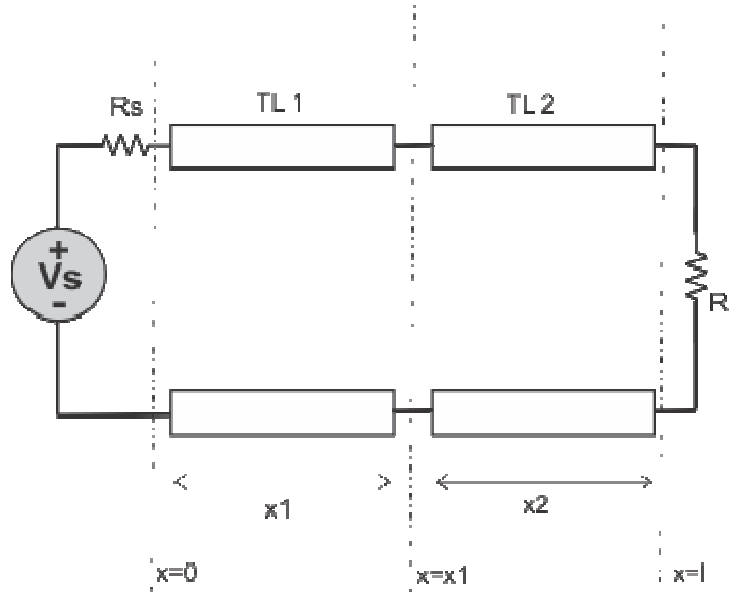
Figure 16: Assumed TL geometry for explaining the TL solver algorithm.

The voltage and current across each TL are given by Telegrapher's Eq. (1) and (2), with the characteristic impedance (Z_0) and propagation constant ( ) being different for each segment.

$$\tag{1}$$

$$\underline{\quad\quad} \quad \underline{\quad\quad} \tag{2}$$

Since, the voltage and current distribution over a TL segment is given by the Telegraphers Equations which has two unknowns A and B, the problem essentially becomes that of solving for four unknowns for the two TL segments. The first of the four required equation, which is obtained by equating the voltages at X=0 is given by Eq. (3). The second and third equation can be obtained by equating the voltages and currents in the two TLs at X=x1 and is given by Eq. (4) and (5). The fourth equation is obtained by equation the voltages at X=l, where l is the sum of the two TL lengths, is given by Eq. (6).

$$\underline{\quad\quad\quad} \quad \underline{\quad\quad} \tag{3}$$

$$A_1 e^{-\gamma 1(x1)} + B_1 e^{\gamma 1(x1)} = A_2 e^{-\gamma 2(x1)} + B_2 e^{\gamma 2(x1)} \tag{4}$$

$$\frac{A_1}{Z_{o1}} e^{-\gamma 1(x1)} - \frac{B_1}{Z_{o1}} e^{\gamma 1(x1)} = \frac{A_2}{Z_{o2}} e^{-\gamma 2(x1)} - \frac{B_2}{Z_{o2}} e^{\gamma 2(x1)} \tag{5}$$

$$A_2 e^{-\gamma 2(l)} + B_2 e^{\gamma 2(l)} = \left(\frac{A_2 e^{-\gamma 2(l)}}{Z_{o2}} - \frac{B_2 e^{\gamma 2(l)}}{Z_{o2}} \right) R_L \tag{6}$$

These four equations can be setup to obtain a system of the form AX=B, given by Eq. (7).

$$\begin{bmatrix} e^{-\gamma 1(0)} + \frac{R_S e^{-\gamma 1(0)}}{Z_{o1}} & e^{\gamma 1(0)} - \frac{R_S e^{\gamma 1(0)}}{Z_{o1}} & 0 & 0 \\ e^{-\gamma 1(x1)} & e^{\gamma 1(0)} & -e^{-\gamma 2(0)} & -e^{\gamma 2(x1)} \\ \frac{e^{-\gamma 1(x1)}}{Z_{o1}} & -\frac{e^{\gamma 1(x1)}}{Z_{o1}} & -\frac{e^{-\gamma 2(x1)}}{Z_{o2}} & \frac{e^{\gamma 2(x1)}}{Z_{o2}} \\ 0 & 0 & e^{-\gamma 2(x2)} - \frac{R_L e^{-\gamma 2(l)}}{Z_{o2}} & e^{\gamma 1(l)} + \frac{R_L e^{\gamma 2(l)}}{Z_{o2}} \end{bmatrix} \begin{bmatrix} A_1 \\ B_1 \\ A_2 \\ B_2 \end{bmatrix} = \begin{bmatrix} V_S \\ 0 \\ 0 \\ 0 \end{bmatrix} \tag{7}$$

The algorithm has been programmed to plot the resulting voltages and currents and for demonstrational purposes we show the results in Figure 17 for the following parametric values: V_G, R_G and R_L are 1Vp, 50Ω and 25Ω respectively, the characteristic impedance for TL1 and TL2 are 50Ω and 35.36Ω respectively, and the TL lengths are λ and $\lambda/4$ respectively.
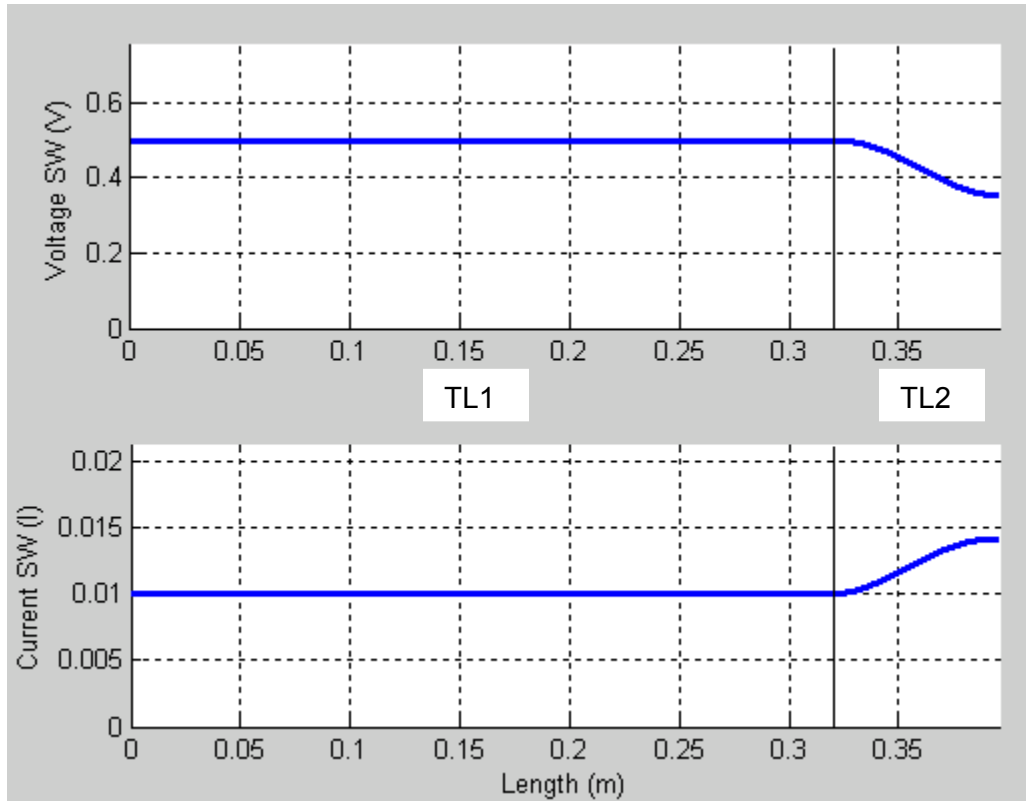
Figure 17: Demonstration of the TL solver algorithm utilizing a λ/4 transformer for TL2 for matching a 25Ω load to 50Ω system.

It should be noted that current and voltage waves displayed as output by the algorithm are standing waves i.e. they represent the envelope of the voltage and current amplitudes across the length of the TL system. The results of Figure 17 can be interpreted easily realizing that TL2 is a lambda quarter transformer and hence is able to transform the load of 25Ω to match the 50Ω system and hence result in a VSWR of 1 across TL1.

3.2   Laser TL Model

The 1-D TL models differ from each other mainly in their method of excitation and the assumed geometry. The two main types of excitations are that of the side driven and centrally driven laser. In side driven lasers the laser is excited by two RF sources, which are identical and exactly in phase, from either end. For a centrally driven laser, the laser is excited by a RF source which is placed exactly in the centre of the laser and hence either half of the laser is assumed to be symmetric about the axis of excitation. An example configuration for a three segment TL model for a side driven laser and centrally drive laser is shown in Figure 18 and Figure 19 respectively.

3.2.1   Side Driven Laser Model

Figure 18: Side driven laser TL segment model.

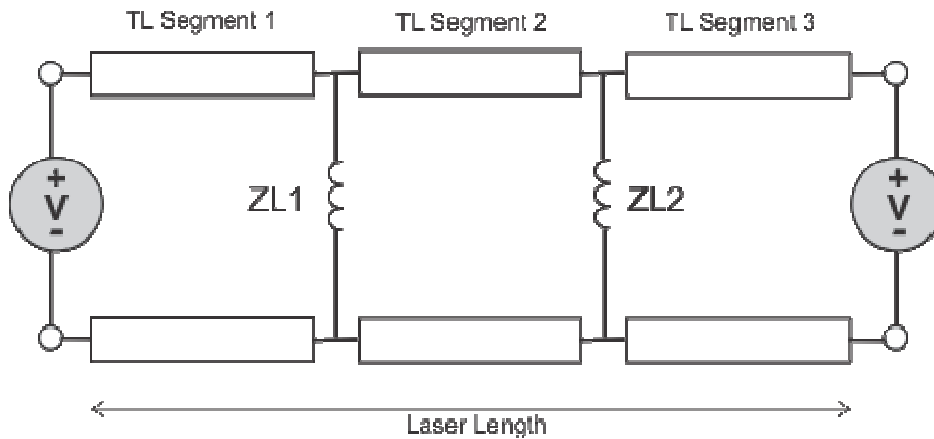The Voltage and Current profiles in each of the segments are given by Eq. (8) and (9). The propagation constant and characteristic impedance, γ and Z_0 are found using Eq. (10) and (11), where R, L, G and C are TL parameters determined by the laser material, geometry and Vitruk's discharge model.

$$(8)$$

$$I_K(x) = \frac{A_K}{Z_0}e^{-\gamma x} - \frac{B_K}{Z_0}e^{\gamma x} \tag{9}$$

Where,

$$Z_{0K} = \sqrt{\frac{(R+iwL)}{(G+iwC)}} \tag{10}$$

$$\gamma_K = \sqrt{(R+iwL)(G+iwC)} \tag{11}$$

The values of R and L are independent of the discharge conditions and hence are the same for all segments and are found using Eq. (12) and (13).

$$R = \frac{2R_S}{W} \tag{12}$$

$$L = \frac{\mu_0 d}{W} \tag{13}$$

Where, w is the electrode width and d is the electrode gap and R_S is the sheet resistance of the slab material. The TL parameters G and C are functions of the discharge current density (J_D) and are found numerically using the Laser Discharge model put forth by *Vitruk et al.* [7] and which is presented in section 2.4.3.

3.2.2   Centrally Driven Laser Model

A symmetric TL model for a centrally driven laser with four segments is shown below. This model has four segments compared with three segments for the side driven laser of similar length, since the Voltage Source has been attached in the middle and has divided the center segment into two. Further two termination inductors have been used as well and this has increased the number of total inductors to four.
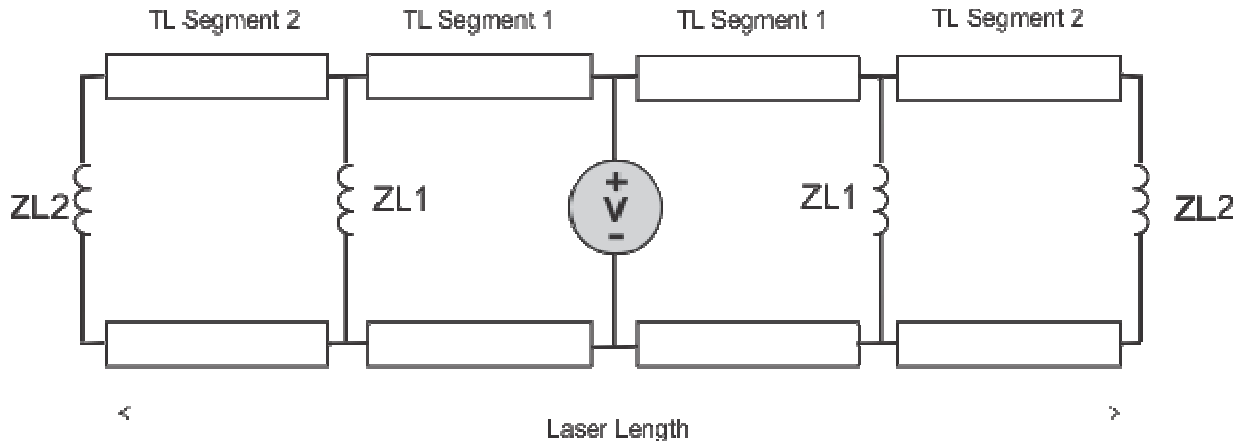
Figure 19: Centrally driven laser TL segment model.

Since the voltage at the center of the laser is determined by the voltage source the voltages and currents in left half of the laser are independent of the voltages and currents in the right half of the laser and vice versa. This result indicates that that the model can be divided into two halves where each half can be solved separately or in other words we would need to only solve for half the circuit to obtain the overall solution.

3.3 Algorithm Steps

The TL parameters G and C are function of J_D (see Section 2.4.3), the vertical current density between the two slabs, which in turn is a function Voltage profile along the laser length. Hence the voltage and current profile solutions along the laser length will result in J_D which was used to calculate G and C in the first place. Hence Vitruk's Discharge model can be incorporated in to our TL solver algorithm by assuming an initial J_D value and by passing the resulting J_D back into G and C in the next iterative step and iterating until the input and output J_D values are close enough to indicate convergence. The algorithm for predicting 1-D voltage and current profiles in

the laser is based on the algorithm put forth in [2] and can be broken down into the following iterative steps.

1. Assume J_D for each segment

2. Using J_D find Z_D for each segment

3. Using J_D calculate G and C for each segment

4. Solve for A_K and B_K for (1) and (2)

5. Recalculate J_D, by using the Average segment Voltage and Z_D using Eq. 14

$$\underline{\qquad\qquad}\qquad\qquad\qquad\qquad(14)$$

6. Stop if the J_D is the same as the last J_D value, otherwise go to step 2

3.3.1 Solving for A_K and B_K

In a simple case in which two lumped inductors are used, we will have three TL segments and six unknowns (A_1, B_1, A_2, B_2, A_3, B_3) as can be seen in Figure 20.
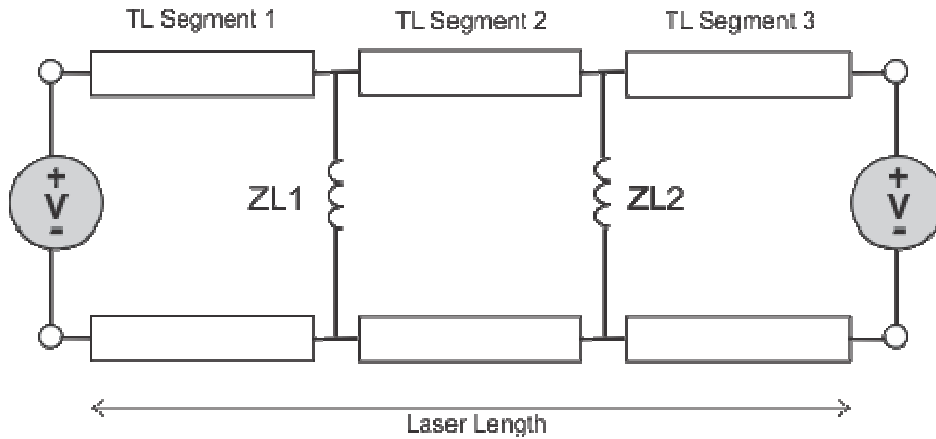

Figure 20: Centrally driven laser TL segment model.

The laser model can be solved for A_K and B_K using the six boundary condition equations (two for each TL segment) which can be easily obtained for the three TL segments.

Boundary conditions at X=0,

$$V_{LHS} = A_1 e^{-\gamma 1(0)} + B_1 e^{\gamma 1(0)} \tag{15}$$

Boundary condition at X=x1, where x1 = segment length,

$$A_1 e^{-\gamma 1(x1)} + B_1 e^{\gamma 1(x1)} = A_2 e^{-\gamma 2(x1)} + B_2 e^{\gamma 2(x1)} \tag{16}$$

$$\frac{A_1}{Z_{o1}} e^{-\gamma 1(x1)} - \frac{B_1}{Z_{o1}} e^{\gamma 1(x1)} = \frac{A_1}{Z_{L1}} e^{-\gamma 2(x1)} + \frac{B_1}{Z_{L1}} e^{\gamma 2(x1)} + \frac{A_2}{Z_{o2}} e^{-\gamma 2(x1)} - \frac{B_2}{Z_{o2}} e^{\gamma 2(x1)} \tag{17}$$

Boundary condition at X=x2, where x2 = 2 × segment length,

$$A_2 e^{-\gamma 2(x2)} + B_2 e^{\gamma 2(x2)} = A_3 e^{-\gamma 3(x2)} + B_3 e^{\gamma 3(x2)} \tag{18}$$

$$\frac{A_2}{Z_{o2}} e^{-\gamma 2(x2)} - \frac{B_2}{Z_{o2}} e^{\gamma 2(x2)} = \frac{A_2}{Z_{L2}} e^{-\gamma 2(x2)} + \frac{B_2}{Z_{L2}} e^{\gamma 2(x2)} + \frac{A_3}{Z_{o3}} e^{-\gamma 3(x2)} - \frac{B_3}{Z_{o3}} e^{\gamma 3(x2)} \tag{19}$$

Boundary condition at X=l, where l =length of the electrode,

$$V_{RHS} = A_3 e^{-\gamma 3(l)} + B_3 e^{\gamma 3(l)} \tag{20}$$

Hence we have six unknowns for six equations. These unknowns can then be solved in MATLAB by setting up the six equations in a system of the form given below.

$$AX = B \tag{21}$$

Where A is a 6x6 matrix, X is a 6x1 matrix and B is a 6x1 matrix, as shown below for an example of a three segment laser.

$$A = \begin{bmatrix} e^{-\gamma 1(0)} & e^{\gamma 1(0)} & 0 & 0 & 0 & 0 \\ e^{-\gamma 1(x1)} & e^{\gamma 1(x1)} & -e^{-\gamma 2(x1)} & -e^{\gamma 2(x1)} & 0 & 0 \\ \left(\frac{1}{Z_{o1}} - \frac{1}{Z_{L1}}\right) e^{-\gamma 1(x1)} & -\left(\frac{1}{Z_{o1}} + \frac{1}{Z_{L1}}\right) e^{\gamma 1(x1)} & -\frac{1}{Z_{o2}} e^{-\gamma 2(x1)} & \frac{B_2}{Z_{o2}} e^{\gamma 2(x1)} & 0 & 0 \\ 0 & 0 & e^{-\gamma 2(x2)} & e^{\gamma 2(x2)} & -e^{-\gamma 3(x2)} & -e^{\gamma 3(x2)} \\ 0 & 0 & \left(\frac{1}{Z_{o2}} - \frac{1}{Z_{L2}}\right) e^{-\gamma 2(x2)} & -\left(\frac{1}{Z_{o2}} + \frac{1}{Z_{L2}}\right) e^{\gamma 2(x2)} & -\frac{1}{Z_{o3}} e^{-\gamma 3(x2)} & \frac{1}{Z_{o3}} e^{\gamma 3(x2)} \\ 0 & 0 & 0 & 0 & e^{-\gamma 3(l)} & e^{\gamma 3(l)} \end{bmatrix}$$

$$X = \begin{bmatrix} A_1 \\ B_1 \\ A_2 \\ B_2 \\ A_3 \\ B_3 \end{bmatrix}$$

$$B = \begin{bmatrix} V_{LHS} \\ 0 \\ 0 \\ 0 \\ 0 \\ V_{RHS} \end{bmatrix}$$

A function which solves the aforementioned system of equations for any number of line segments and lumped inductors can be implemented in MATLAB. It should also be noted that the first and the last row of the matrix constitute the boundary conditions and these equations can be modified for including more complex excitation sources into the model. For example if required the voltage source resistances can be incorporated into the model by replacing Eq. (15) and (20) with Eq. (22) and (23).

$$V_{Laser,x} = \left(A_1 e^{-\gamma 1(0)} + B_1 e^{\gamma 1(0)}\right) = V_{LHS} - \left(\frac{A_1 e^{-\gamma 1(0)}}{Z_{o1}} - \frac{B_1 e^{\gamma 1(0)}}{Z_{o1}}\right) R_{LHS} \tag{22}$$

$$V_{Laser,l} = \left(A_3 e^{-\gamma 3(l)} + B_3 e^{\gamma 3(l)}\right) = V_{RHS} + \left(\frac{A_3 e^{-\gamma 3(l)}}{Z_{o3}} - \frac{B_3 e^{\gamma 3(l)}}{Z_{o3}}\right) R_{RHS} \tag{23}$$

Where, RLHS and RRHS are the left and right source resistances respectively.

A very similar analysis setup can be used for a centrally driven laser utilizing its symmetric nature; as the centrally driven laser is symmetric about the excitation source, this problem can be solved by considering the two halves as being two parallel TL systems.

3.4 1-D Model Results

Two separate MATLAB scripts were developed for the centrally driven and the side driven laser. Even though the overall algorithms are very similar for both cases, there are two major differences; the matrix used to solve for A_K and B_K is set up differently for both cases and secondly the symmetry conditions of a centrally excited laser require that only half the circuit is solved.

3.4.1 Preliminary Side Driven Laser Model Results

The side driven laser model has two ideal perfectly in-phase voltage sources and utilizes the laser parameters from [2]. The laser had a length of 1m, width of 5cm, electrode gap of 3mm and electrode surface area of 500cm^2. The gas mixture was He:N2:C02=3:1:1+5%Xe and an excitation frequency of 82 MHz. For the first simulation two 14.5nH inductors were used to divide the 1m laser into three equal segments. The simulation with the parameters mentioned above converged to obtain the voltage and current profiles shown in Figure 21 and an overall power loading of 8.3W/cm^2. As can be seen the 14.5nH inductors resulted in a fairly uniform voltage profile along the laser length.

Figure 22 shows the voltage profiles for each iteration and as can be seen the Voltage profile for the first iteration was non-uniform but as the algorithm iterated the current density increased until the input and output values converged, resulting in linearized voltage profile along the laser as the values picked had been optimized for the specified laser parameters.
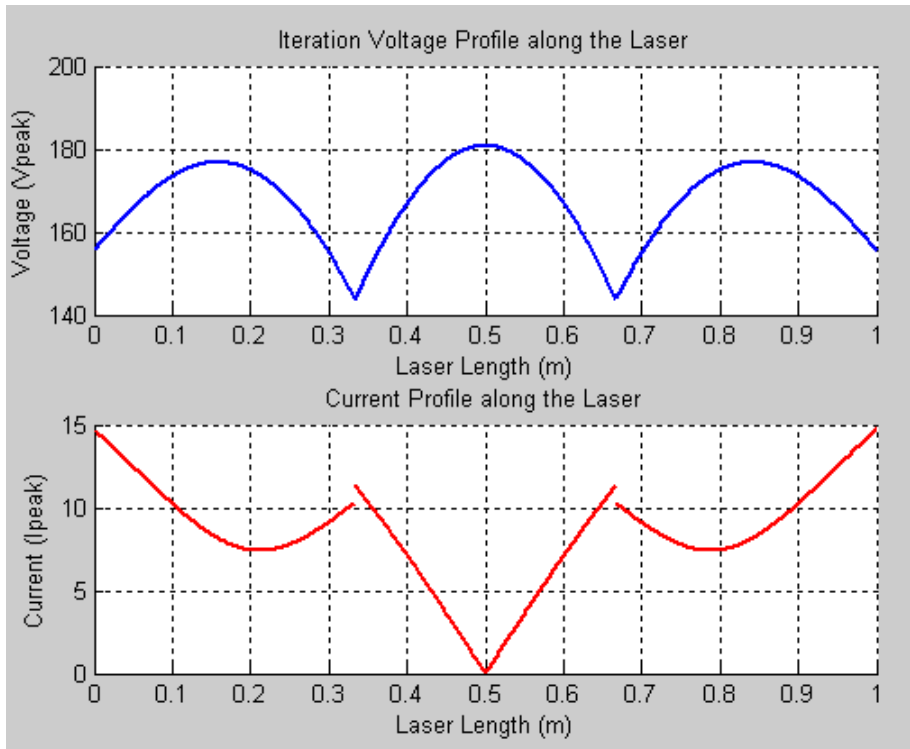
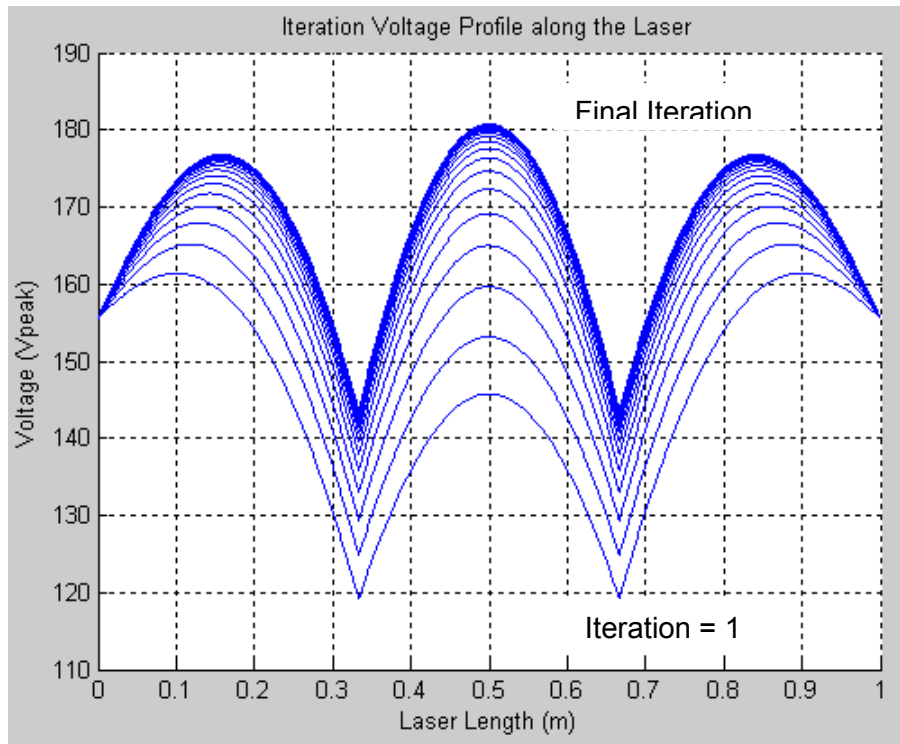Figure 21: Voltage and Current profiles for two 14.5nH inductors.

Figure 22: Voltage Profiles for each iteration for two 14.5nH inductors.

The current profile from Figure 21 also shows the expected symmetric distribution and the discrete current jumps correspond with the position of the lumped external Inductors. The algorithm has the capability of handling a large number of external inductors with specified installation positions along the length of the laser. As an example the earlier simulation was repeated after increasing the number of inductors to four while keeping the inductance values at 14.5nH. The resulting voltage and Current profile are shown in Figure 23.
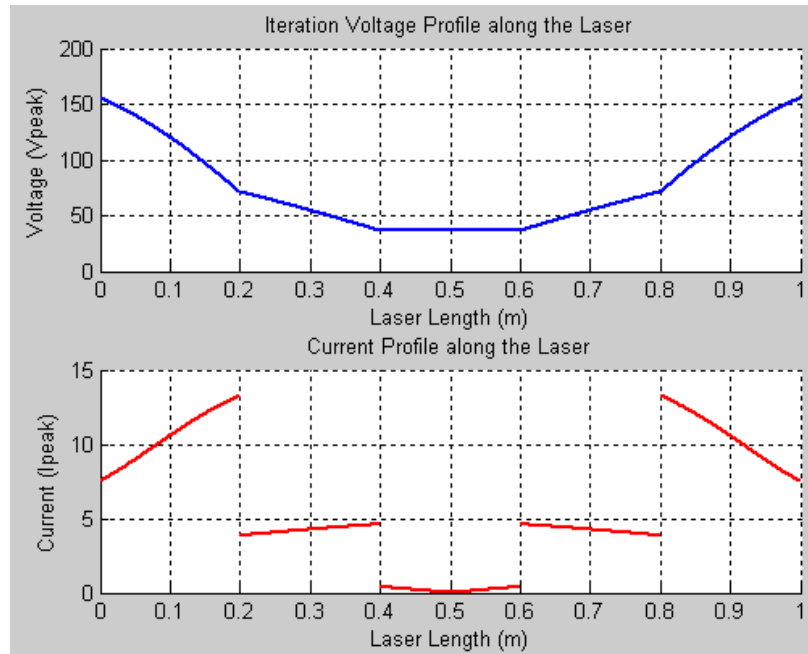

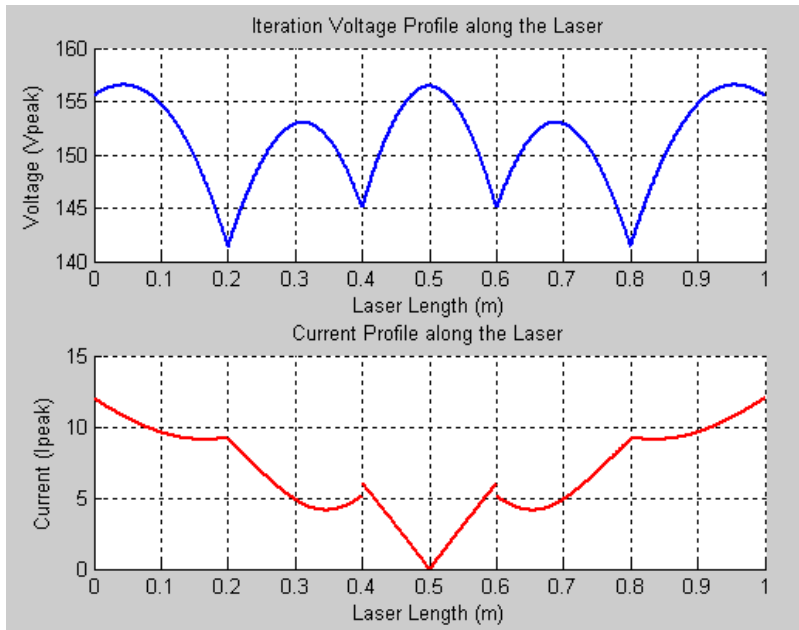Figure 23: Voltage and Current profiles for four 14.5nH inductors

Figure 24: Voltage and current profiles for four 28.5nH inductors.

As expected the voltage profile became non-linear and the voltages in the middle TL segment dipped as the number of inductors were arbitrarily increased while keeping the inductance values the same. The more uniform voltage profile for four inductors is shown in Figure 24 and was obtained when the inductor values were changed to 28.5nH. To show the extent of the capability of the algorithm or MATLAB the number of inductors on the laser were increased to 16 inductors of 106nH each, and the resulting Voltage and the Current profiles can be seen in Figure 25. It should be noted that this simulation was done only to show the model capability, as a laser having similar power loading and this many inductors will be unstable and impractical.
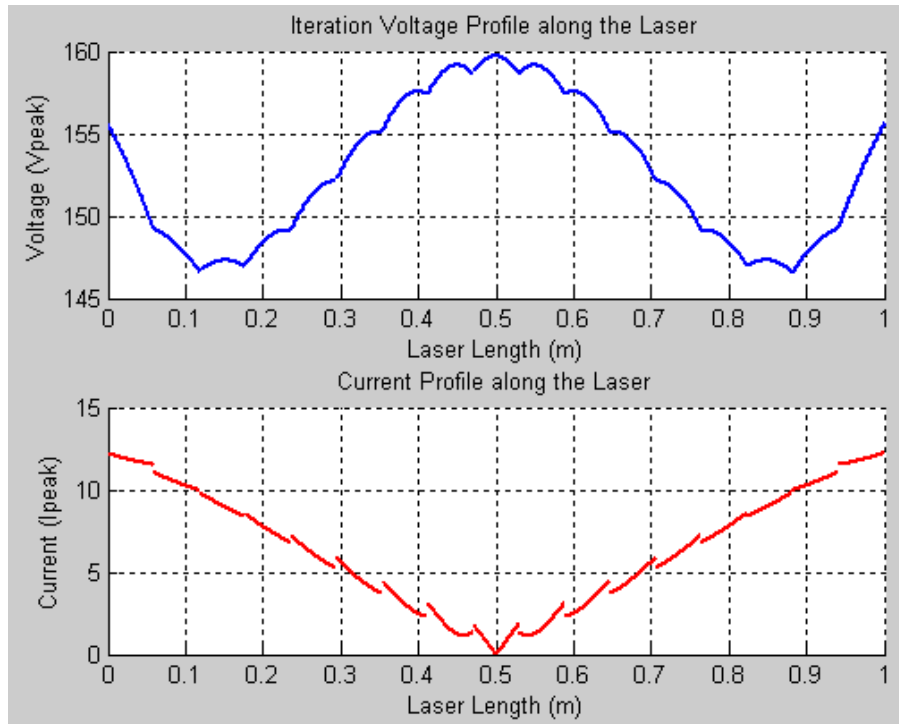
Figure 25: Voltage and current profiles for sixteen 106nH inductors.

3.4.1.1 *Effect of Frequency on voltage profile*

The voltage profile shown in Figure 26 was obtained for a side driven CO_2 laser excited at 110Vrms and having two inductors of 11nH each. The value of 11nH was well matched for a laser excitation frequency of 80MHz. As the excitation frequency was increased the discharge capacitance increased resulting in the undesirable non linear discharge. To improve this nonlinearity the value of the inductors was decreased as is apparent from Eq. (24) which depicts the parallel impedance of an inductor and capacitor. As an example, the simulation was repeated at 90MHz but this time the value of the inductors was varied from 1.1nH to 11nh in steps of 1.1nH and as can be seen in Figure 27 the best case results at 7.7nH at 90MHz instead of 11nH for the operation at 82MHz.
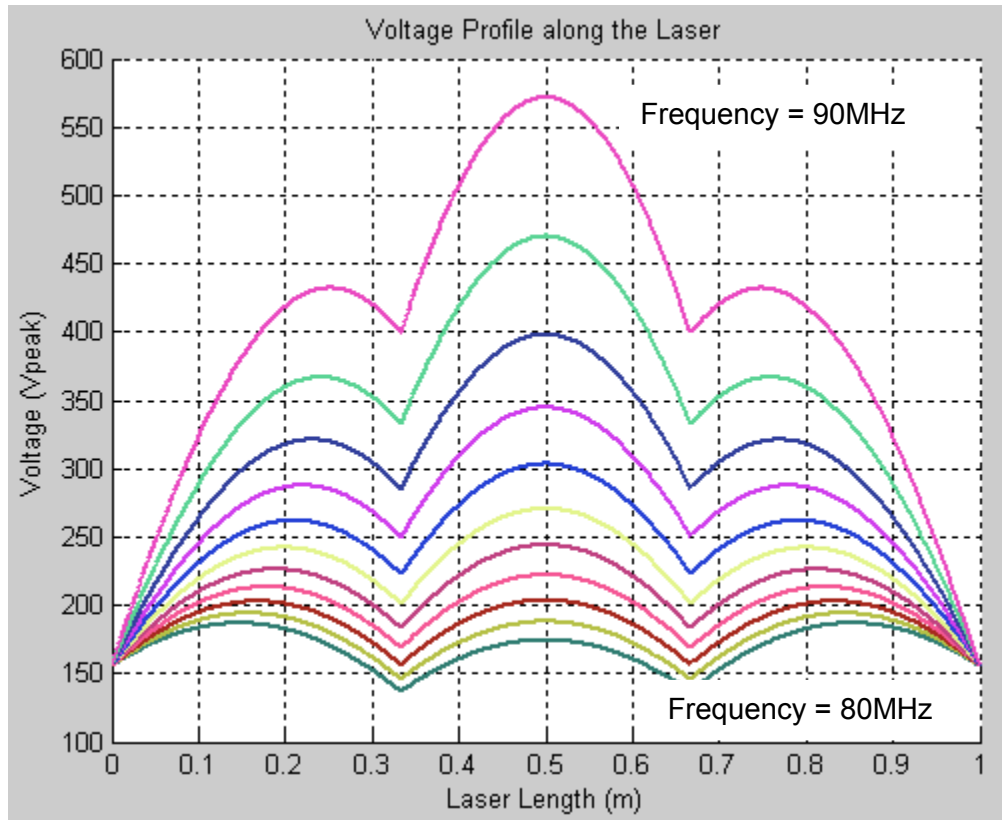
Figure 26: Voltage variation v/s frequency from 80MHz to 90MHz in steps of 1MHz, for two inductors of 11nH each.

$$Z_{parallel} = \frac{1}{jwC} || jwL = j\frac{wL}{1-w^2LC} \tag{24}$$

Figure 27: The effect of inductance variation v/s voltage profile at f=90MHz.

The previous simulation was repeated but this time both the inductors were removed and hence the impedance represented by Eq. (24) decreased with increasing frequency unlike the case with shunt inductors and resulted in highly non-linear and lower voltages as can be shown from Figure 28.

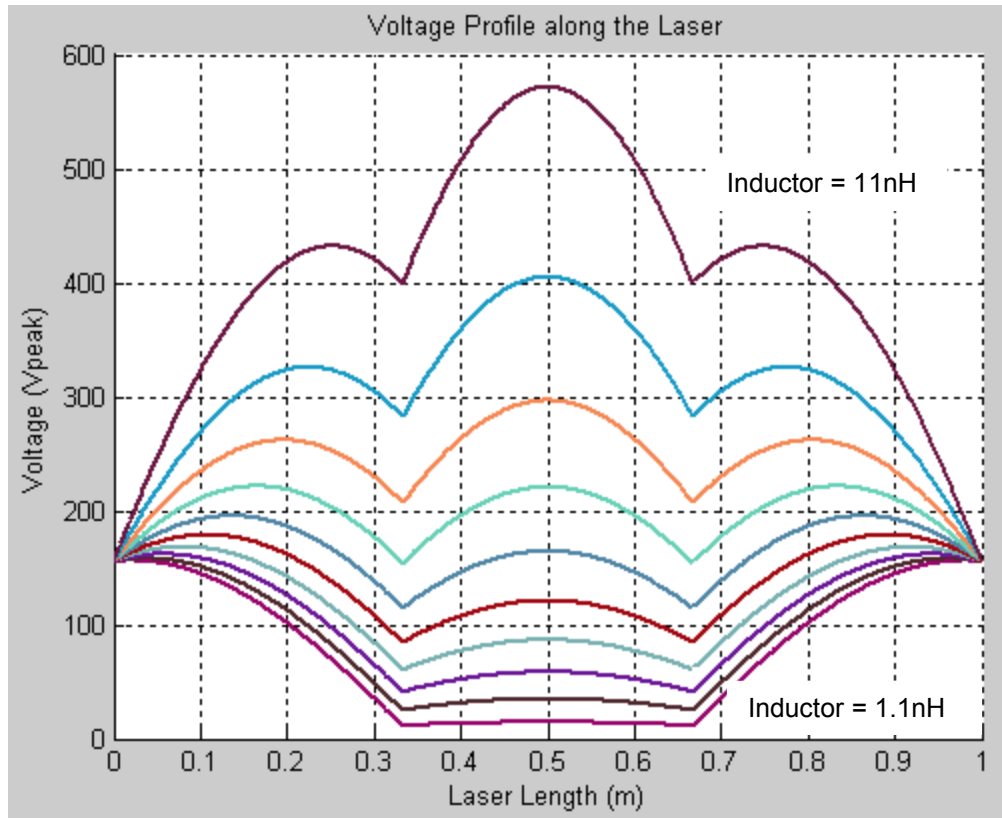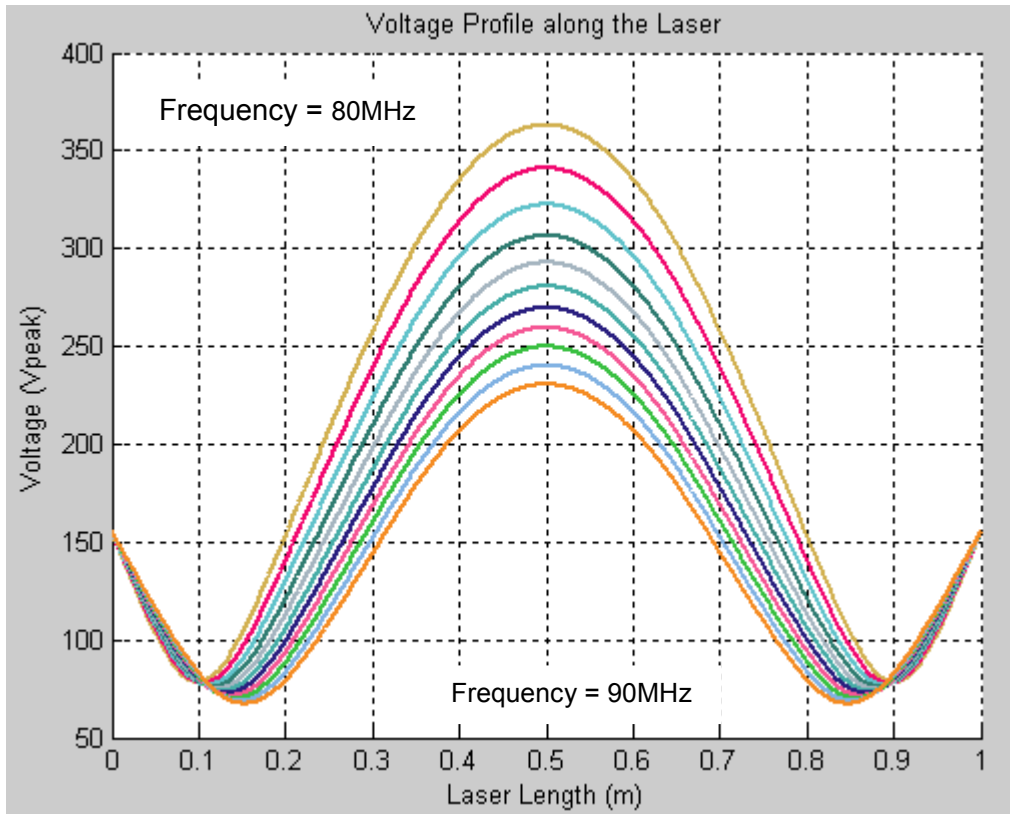Figure 28: Voltage profile variation v/s excitation frequency variation from 80MHz to 90MHz in steps of 1MHz without any inductors.

Lastly we plotted model parameters of interest as a function of the excitation frequency and the results are shown in Figure 29. The average power density increases with the frequency of excitation and it should also be noted that the plasma voltage is quite insensitive to the increasing frequency when compared with the ion sheath voltage.

Figure 29: The average power density and the plasma and ion sheet voltage as a function of excitation frequency.

Having a laser model which is easily configurable allows us to optimize the laser design by doing sensitivity analysis and by running Monte Carlo simulations. The side driven laser is sensitive to the matching effectivene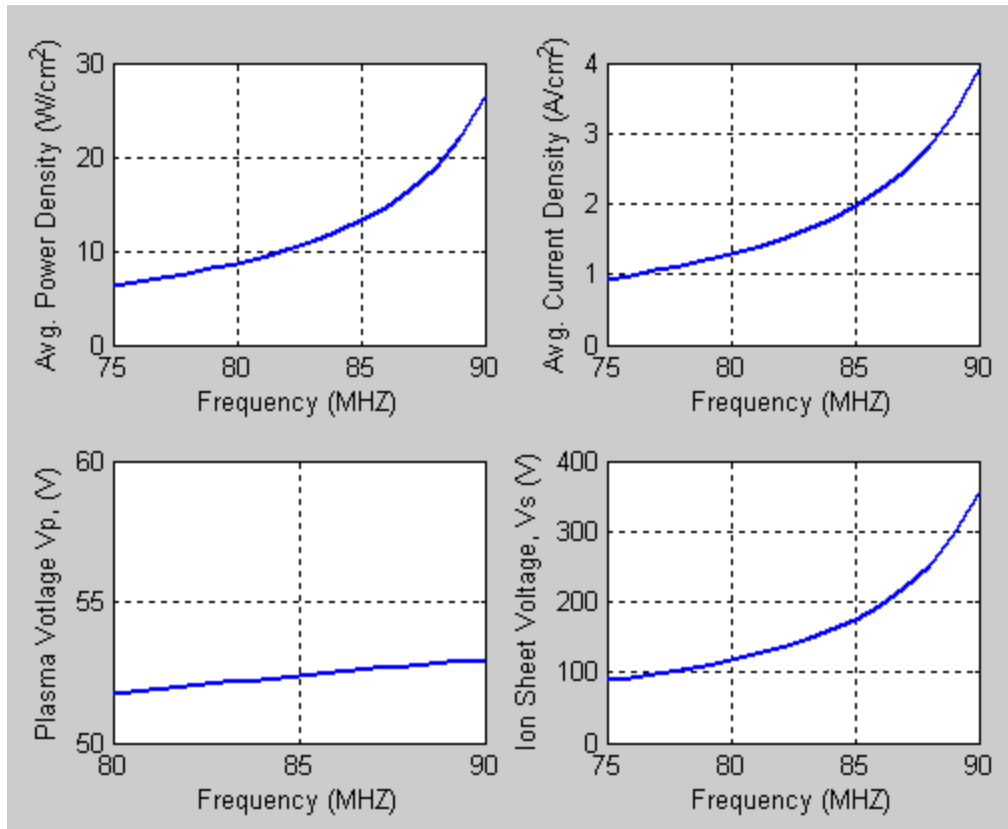ss between the two voltage sources, and care has to be taken to match them closely. A simulation was run in which the sources were mismatched and the results are presented in Figure 32. The symmetry and the non-linearity were fairly low for 1-5% error, but as the mismatch increased to around 10% the nonlinearity increased markedly. The next simulation that we ran was to ascertain a bound on the laser discharge loading due to the 5% inductor tolerance. Such a simulation can be very useful as we can see from the simulation results that (Figure 31) there is a greater than 1000V variation in the laser voltage profile.
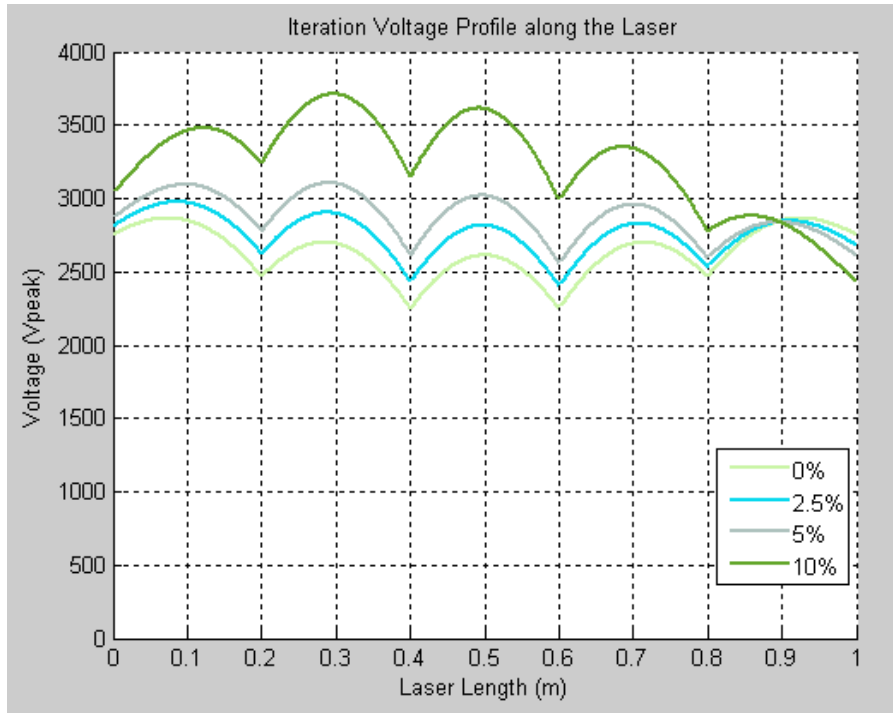
Figure 30: The effect of mismatch between the two voltage sources in a side driven laser.
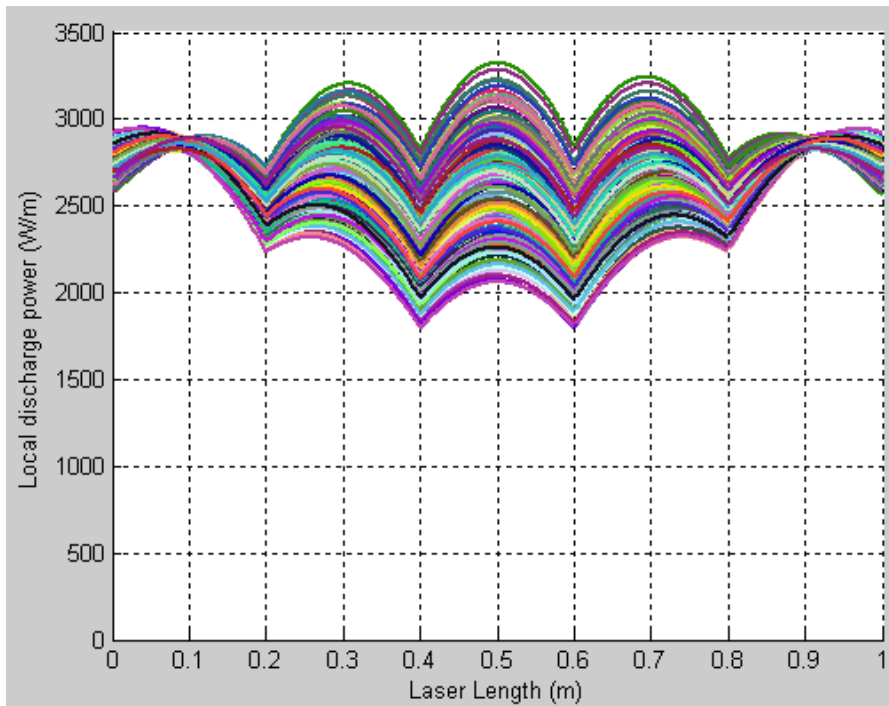

Figure 31: The effect of the 5% inductor tolerance on the laser discharge loading.

3.4.2   Centrally Driven Laser Model Results

For the centrally driven laser we just used a single 110VRMS source and due to the symmetry characteristics solved each circuit half separately. We used a laser which was 70cm in length, 10cm wide and had an electrode gap of 2mm with an excitation frequency of 80MHz. These values were picked so that the simulations were comparable with the laser used in [4]. Figure 32 shows the voltage and current profiles for four 50nH inductors placed along the length of the laser.
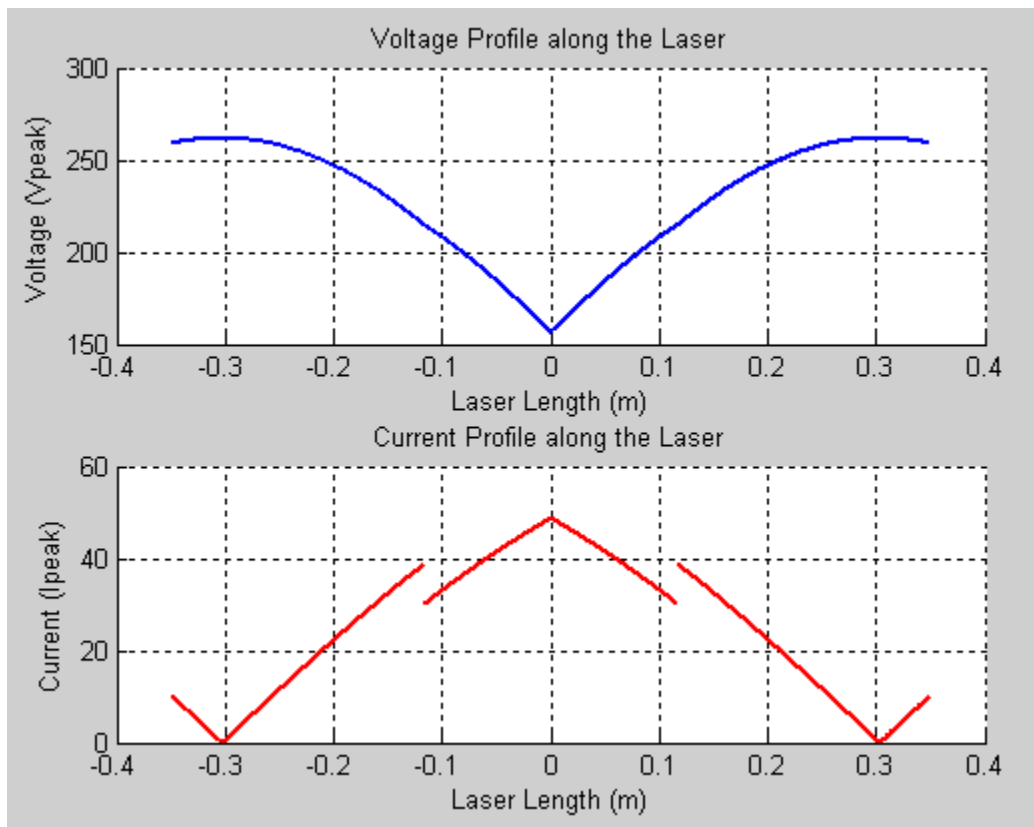
Figure 32: Centrally Driven Laser with four 50nH inductors at f=80MHz.

Next we ran simulations to investigate the effects of having termination inductors on a laser. We plotted the voltages for a 70cm x 10cm and 2mm electrode gap laser from [4], with and without 50nH termination inductors on either ends. Figure 33 shows the placement of two termination inductors results in the reduction of 100V at each of the laser ends, and shows why

inductors and especially termination inductors are an important method of gain discharge linearization for a RF excited slab laser. Also it should be noted that the effect of placing two additional inductors in addition to the termination inductors does not have a big effect as they result in a fairly small reduction in the gain discharge non-linearity.

Figure 33: Comparison of Voltage profile with and without 50nH Inductor terminations.

.

4   Two-Dimensional Model Algorithm

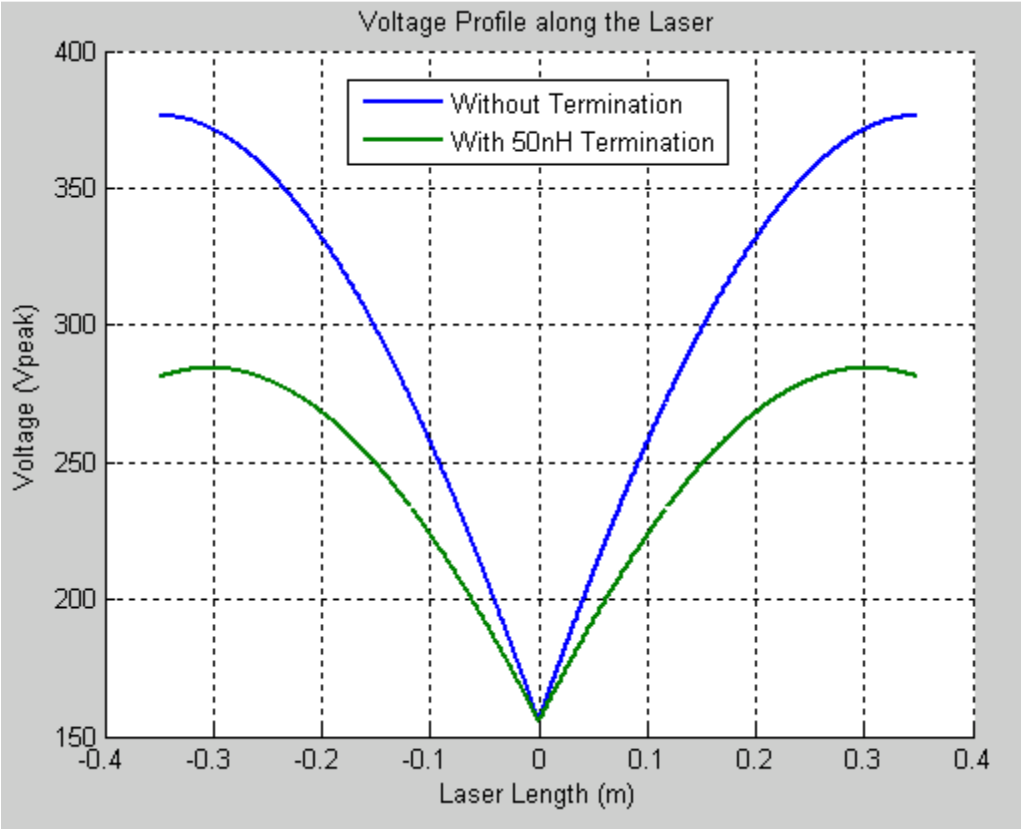A special-purpose 2-D FDTD code was implemented following the approach adopted by *Spindler* [6]. The top electrode in Figure 2 is excited by a RF voltage source of approximately 100MHz, while the bottom plate is grounded. The FDTD model is then implemented as a Transverse Magnetic (TM) wave problem, with the electric field pointing in the Z direction, and the magnetic field components pointing along the X and Y direction. It should be noted that the Cartesian grid used for this FDTD model is in the XY plane, and represents the gas mixture volume between the two plates. *Vitruk's* [2] discharge model is incorporated into the 2-D model in a manner similar to the 1-D implementation (see Section 3.2). The simulation is started without any discharge present, and the resulting voltage amplitudes across the slabs are used to predict the state of the laser discharge parameters, and thereby the resulting permittivity and the conductivity of the gas mixture are updated in the grid for the next iteration. This procedure is repeated until the voltage amplitudes on the slab reach a steady state value and the permeability and conductivity parameters converge to their solution value for a given set of laser parameters.

The algorithm steps can be summarized as following:

1. Initialize variables and laser geometry parameters

2. Solve for magnetic field components, *Hx* and *Hy*

3. Solve for electric field component, *Ez*

4. Update voltage source value

5. Apply boundary conditions

6. Calculate voltage amplitude across the slab

7. Calculate discharge parameters

8. Compute new gas mixture permittivity and conductivity values

9. Go to Step 2 and repeat until steady state voltages occur

The computational code can be altered to add inductors necessary for linearizing the capacitive discharge nature of the CO_2 laser. A step will have to be inserted between Steps 2 and 3 to incorporate the external inductors being used to tune out the discharge capacitances. In this step the inductor currents are updated and the resulting current density term $J_{inductor}$ used in the Ez update equation in Step 3.

Preliminary results of our computational program are reported in Figure 34 and Figure 35, for a CO_2 laser having the following parameters: F= 82MHz, Pressure=135 torr, and Voltage Source: 300Vrms and Gas Mixture: He:N_2:CO_2 = 3 : 1 : 1 + 5% Xe.

In the absence of inductors, as expected the voltage distribution is not optimal as shown in Figure 34. This high degree of nonlinearity leads to an unstable discharge and reduced efficiency. It should also be noted that majority of the plots presented in this section were obtained by using a Cartesian grid made up of 22 x 100 Yee cells.
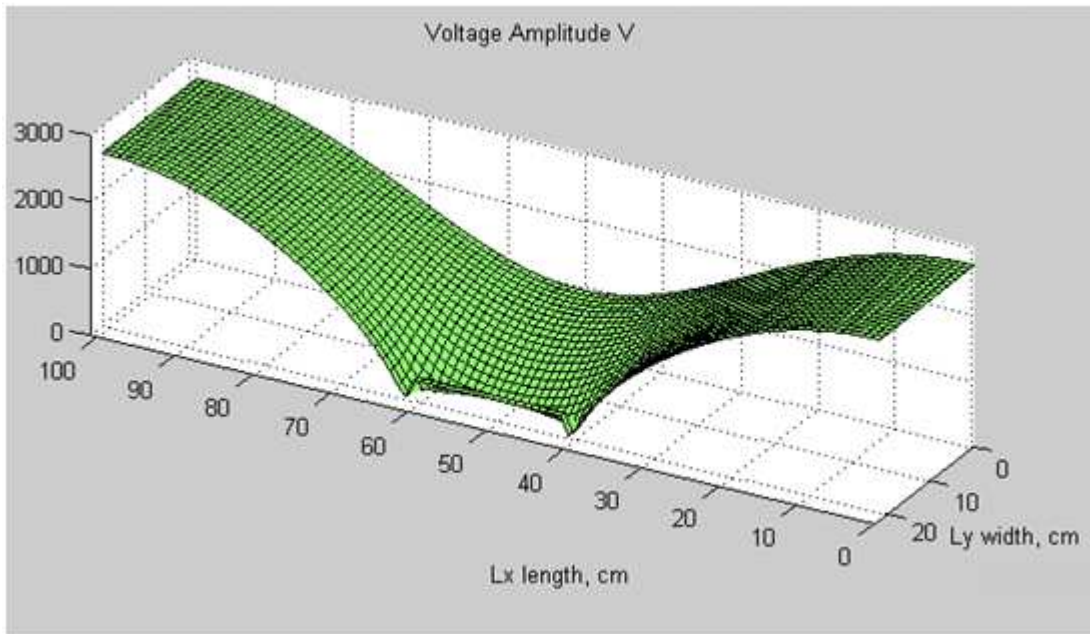

Figure 34: Voltages between the slab, without inductors.

The algorithm allows experimentation with inductor placement and size to linearize the spread of the voltage standing waves between the two electrodes. The optimal case was found when ten inductors were added to our simulation (as shown in [6]), six on the side opposite to the voltage source (20cm apart), and four on the side of the voltage source. The resulting standing wave amplitudes can be seen in Figure 35. As is evident, the voltage distribution in the presence of shunt inductors is considerably more linear, and a cross sectional plot depicting the voltage amplitude profiles for the two cases is shown in Figure 36.
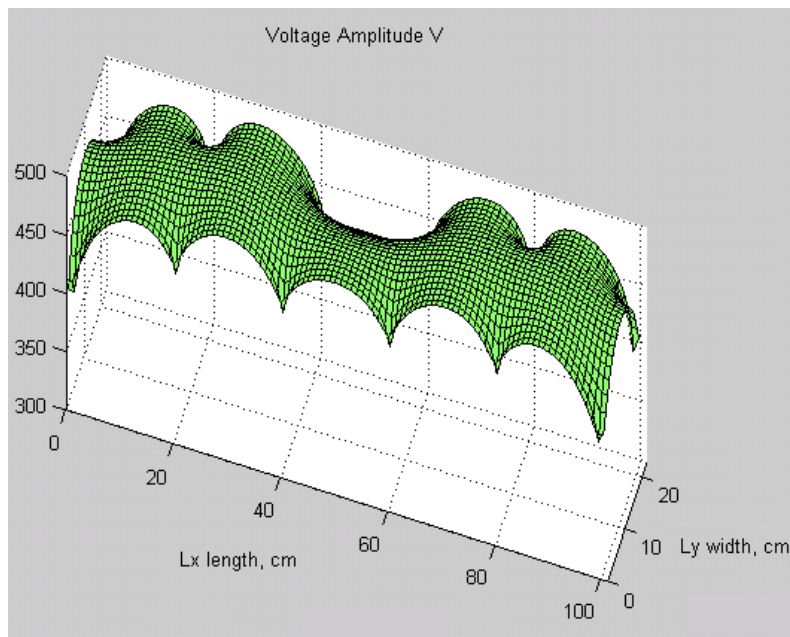

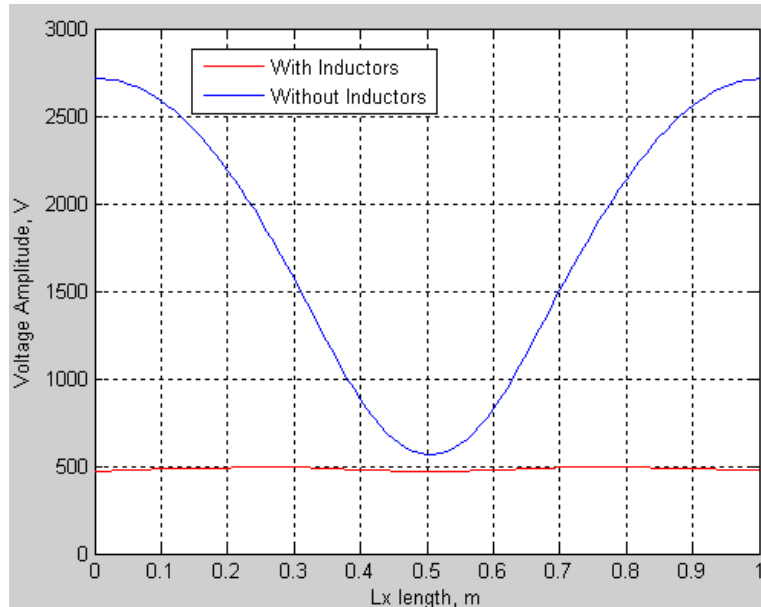Figure 35: Voltages on the slab with inductors.

Figure 36: Cross sectional plot of the voltage amplitude profiles at Ly=11cm (11cm from edge),

showing the effectiveness of shunt inductors in linearizing the laser discharge.

For lower aspect ratios the 2-D FDTD model essentially reduces to a 1-D model. Figure 37 & Figure 38 were obtained for a laser which was 2cm wide, and all other parameters were the same as for the earlier simulations and also picked from [3]. As Figure 35 shows the voltages collapse in the absence of the inductors due to the high discharge loading, where as in the presence of termination inductors we are able to tune out the discharge capacitance and have a more linear discharge profile as seen in Figure 38. The uniformity of the voltages along the laser width should be noted, as this shows that for lower aspect ratios 1-D models may be sufficient. Figure 39 shows a cross sectional plot, which effectively shows the effectiveness of shunt inductors in voltage linearization in CO_2 lasers.
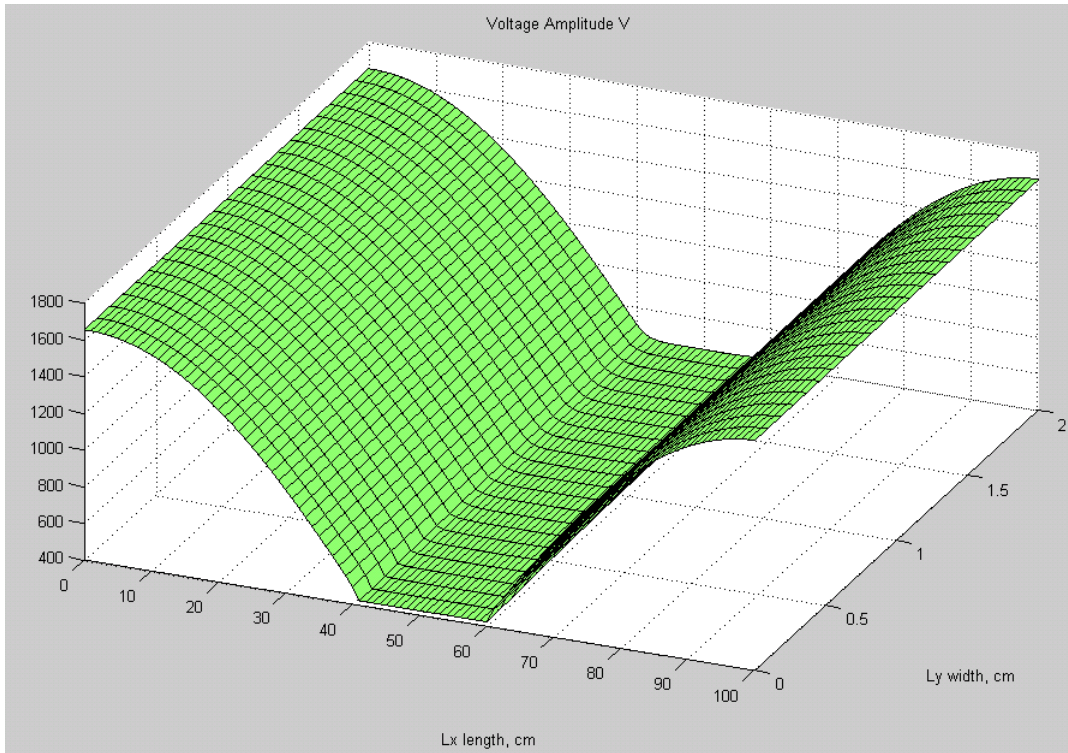
Figure 37: A low aspect ratio simulation (0.02) in absence of shunt inductors.
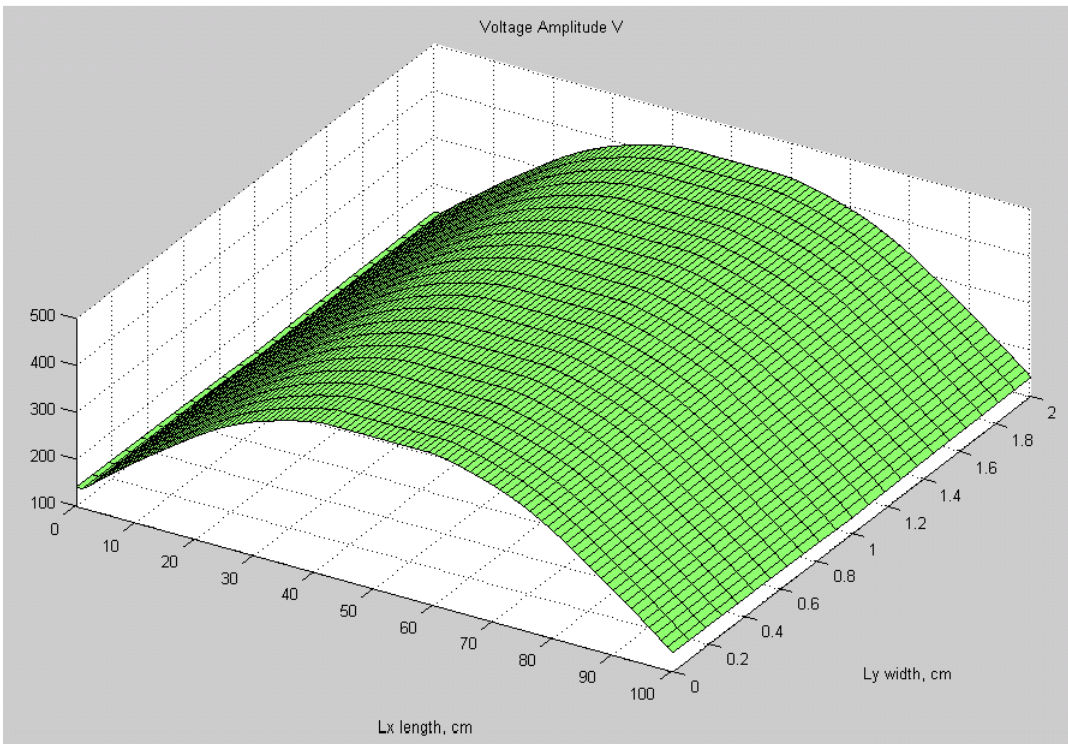
Figure 38: A low aspect ratio simulation (0.02) in presence of 15nH termination inductors.
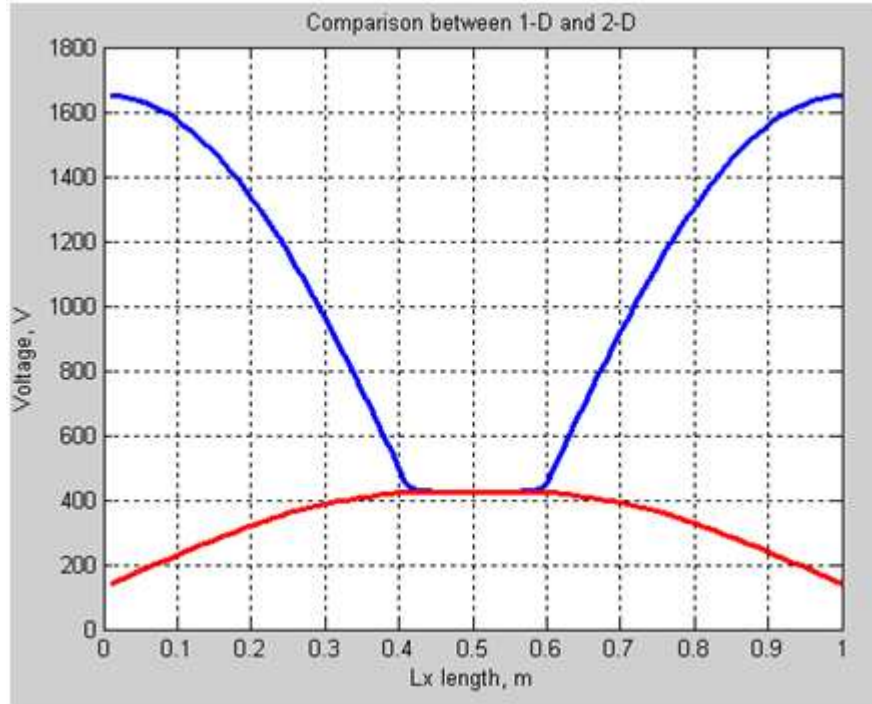
Figure 39: Cross sectional plot showing the result of using two 15nH termination inductors.

4.1 Voltage Excitation

Transverse RF excitations are of interest as they require lower voltages than for a longitudinal discharge due to the smaller size of the transverse separation between the bottom and the top slabs. Hence for a longitudinal discharge much higher voltages need to be used for the same power of laser discharge. The behavior of discharge in a laser is very different from that of a simple resistor as depicted in Figure 40.
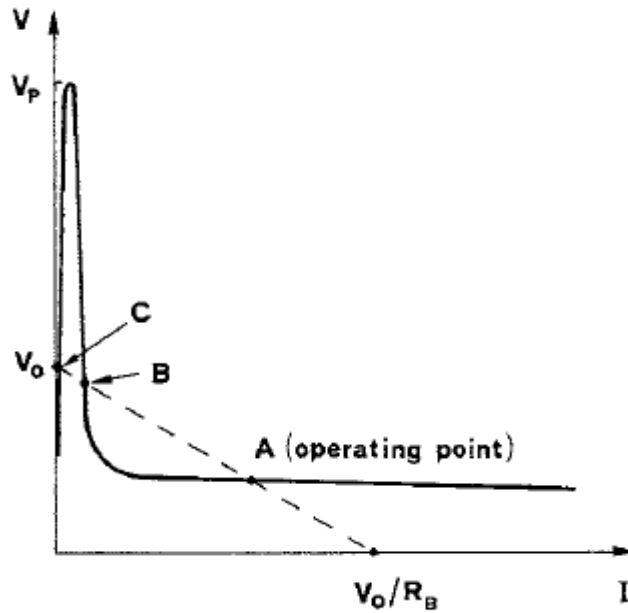
Figure 40: VI characteristics of the Laser Discharge and the Voltage Source with a series

resistor [18].

The solid line represents the VI characteristics of the laser discharge, while the dotted line represents the VI characteristics of the voltage source with a series resistor called the ballast resistor (R_B) added. And as can be seen that point A represents the operating point of the laser at which the voltage is insensitive to the current fluctuations. It should be noted that the laser can obtain a stable equilibrium at points A and C, but not a B, which represents an unstable equilibrium point. It also has to be noted that for the laser to operate at point A the voltage peak of V_P, which is much higher than the operating points, needs to be applied otherwise the voltage stabilizes at point C [18]. The value of the ballast resistor R_B also plays an interesting role as it moves the operating point A to the desired power discharge level.

4.1.1 Modeling Voltage Sources in FDTD

The choice of voltage source being used in the code is of vital importance. In general there are two types of voltage sources that are used in FDTD simulations and they are commonly referred to as hard sources and soft sources.

a)   Hard Source - In this source implementation, the calculated values for the E-field at the source cell are just replaced by the source voltage values. This type of a source is not transparent and results in reflections when any reflected wave reaches back to the source nodes.

b)   Soft Impedance Source – A soft impedance source or any lumped component can easily be added to the FTDT code using Eq. (25). It can be derived using Ampere's current law with the Maxwell's correction, as shown in [20]. A detailed derivation is presented in Appendix A.

$$E_Z^{n+1} = \left(\frac{1-\frac{\Delta t\sigma}{2\varepsilon}-C}{1+\frac{\Delta t\sigma}{2\varepsilon}+C}\right)E_Z^n + \left(\frac{\frac{\Delta t}{\varepsilon}}{1+\frac{\Delta t\sigma}{2\varepsilon}+C}\right)\left(\nabla \times H^{n+\frac{1}{2}}\right) - \left(\frac{\frac{\Delta t}{\varepsilon}}{1+\frac{\Delta t\sigma}{2\varepsilon}+C}\right)\frac{V_{source}}{R_{source}\Delta y\Delta x} \tag{25}$$

where we set

$$c = \frac{\Delta t\Delta z}{2\varepsilon R_{source}\Delta x\Delta y}$$

Next we simulate the model from Figure 35 with a 300Vrms soft source with 50Ω impedance. The resulting voltage profile is shown in Figure 41. The laser discharge is a nonlinear function of the discharge current and hence the marked reduction in standing voltage wave amplitudes is seen. Hence the 2-D FDTD model allows incorporation of more complex voltage sources.
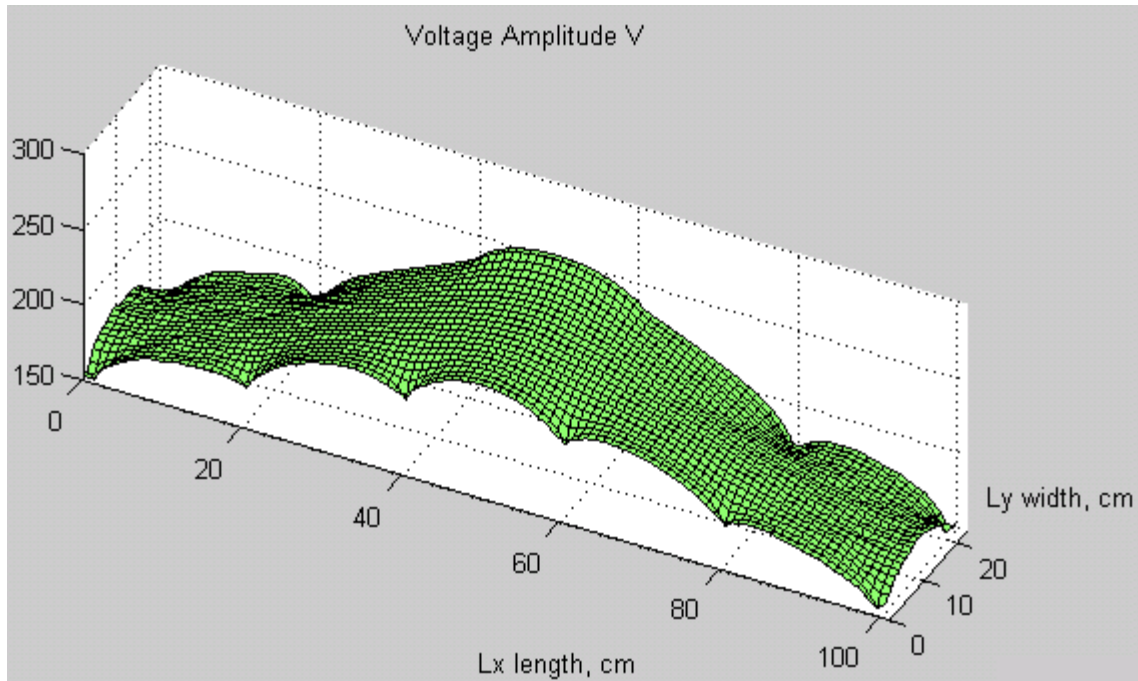
Figure 41: The resulting voltage distribution for a 50Ω impedance soft source as compared to the profile shown in Figure 35 for an ideal source.

4.2 Boundary Conditions

Applying appropriate boundary conditions in a numerical simulation is of vital importance. Initially the Perfectly Magnetic Conductor (PMC) boundary conditions, which provide perfect electric wave reflections, were implemented as advocated in [6]. This seems like a good approximation since the RF losses in a CO_2 laser are very minimal as the optical components used to make the optical resonance cavity for the laser are coated with material which makes them good reflectors. Hence by using this boundary condition it is assumed that the loss in a laser is due to the losses in the discharge itself.

Multilayer dielectric coatings are used on the glass mirrors to increase or decrease reflectivity as desired. This coating is created by evaporating high dielectric constant material, which then forms a thin layer on the substrate. If these layers have alternating high to low refractive indexes and are multiples of one fourth the laser wavelength, the incident and the

reflected electric waves will have the same phase and the electric field at the laser boundary will double [18].

In the Y-dimension, ceramic spacers are used to maintain the electrodes at the same distance throughout their length. Very often alumina ceramic materials are used as slab spacers as they are thermally stable, have low infrared absorption and low dielectric losses at RF frequencies of interest and therefore making them ideal for RF slab lasers [15].

The boundary conditions were next modified in order to account for the ceramic spacers. The original PMC boundary conditions are retained in the X-dimension, while in the Y-dimension they are replaced by extra layers of ceramic material on both sides to simulate the effect of ceramic spacers and at the boundary the metal wall boundary condition was added to simulate the shielded metal casing. Figure 42 shows the effect of adding a 5cm row of alumina ceramic spacers (having a relative permittivity of 9.7) on either side of the laser as shown in Figure 2. The resulting standing wave voltage amplitudes are much lower than earlier throughout the slab, due to the effect of the metallic shielding along the slab length; a marked change in voltage amplitude is observed at the boundary between the laser gas mixture and the ceramic material. Next, a sensitivity analysis was done by varying the width of the ceramic spacers on either side of the laser. The width of the ceramic spacer was changed from 5cm to 20cm in increments of 5cm. The voltage across the slab was more linear as the ceramic spacer width was increased. Figure 43 shows the voltage distribution along the laser width at L_X = 25cm (or 25cm from the laser edge). The voltage distribution along the laser length at L_Y=7cm is shown in Figure 44. As can be seen the voltage in the center of the laser decreases and on the side increases due to the increase in the ceramics spacer width. This is desirable as the voltage variation along the laser is reduced. Hence having anything less than a perfectly reflecting boundary condition results in voltages which are much lower than those predicted by literature with perfectly reflecting boundaries, and under these voltage conditions the discharge properties

are insensitive to the inductors. However what is of much interest is the improvement in voltages due to the increase in the width of the ceramic spacers; this should be investigated further.
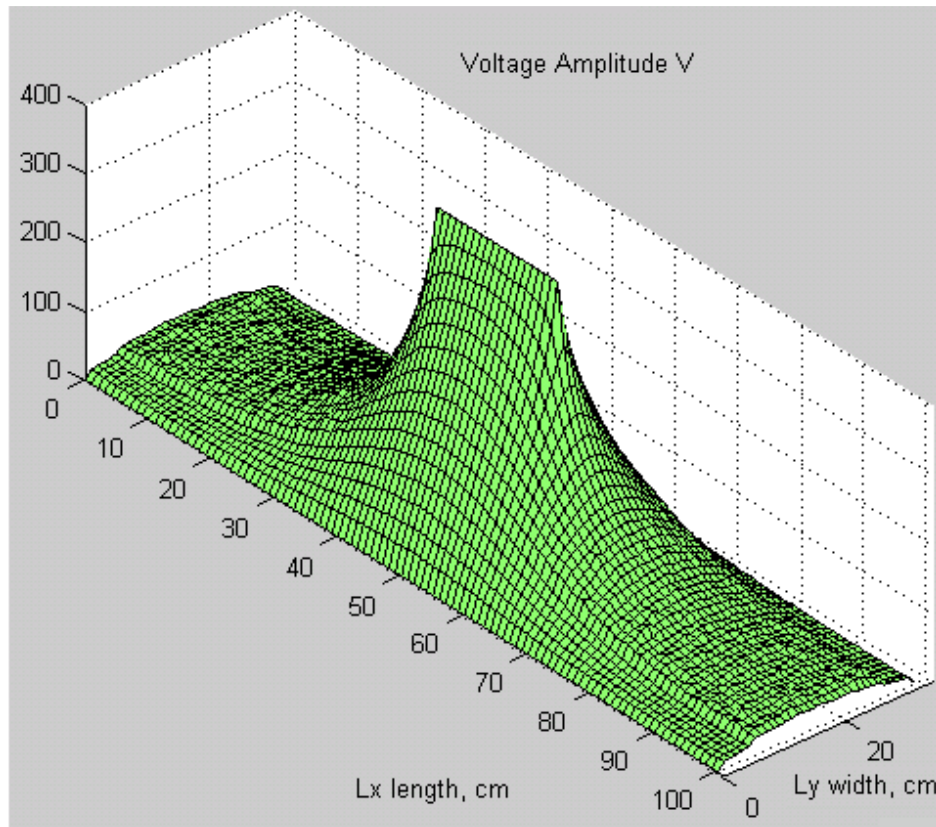

Figure 42: Voltage distribution with ceramic material added on both sides in the Y-dimension followed by metal walls.
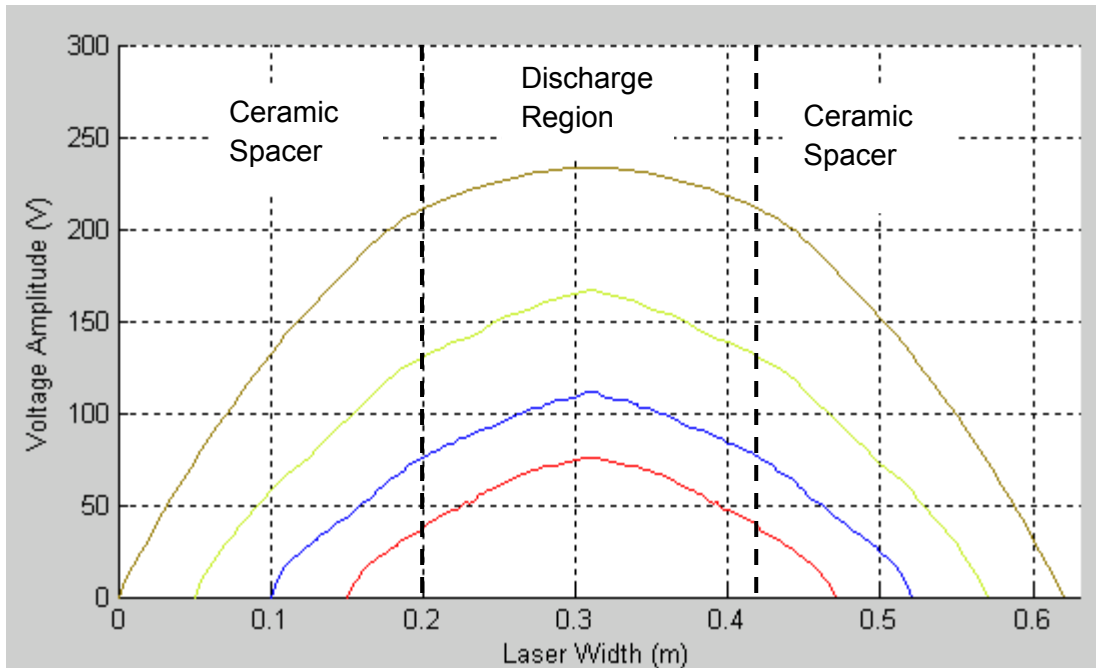
Figure 43: Voltage Distribution along the width at Lx = 25cm, for ceramic spacer widths of 5, 10, 15 and 20cm
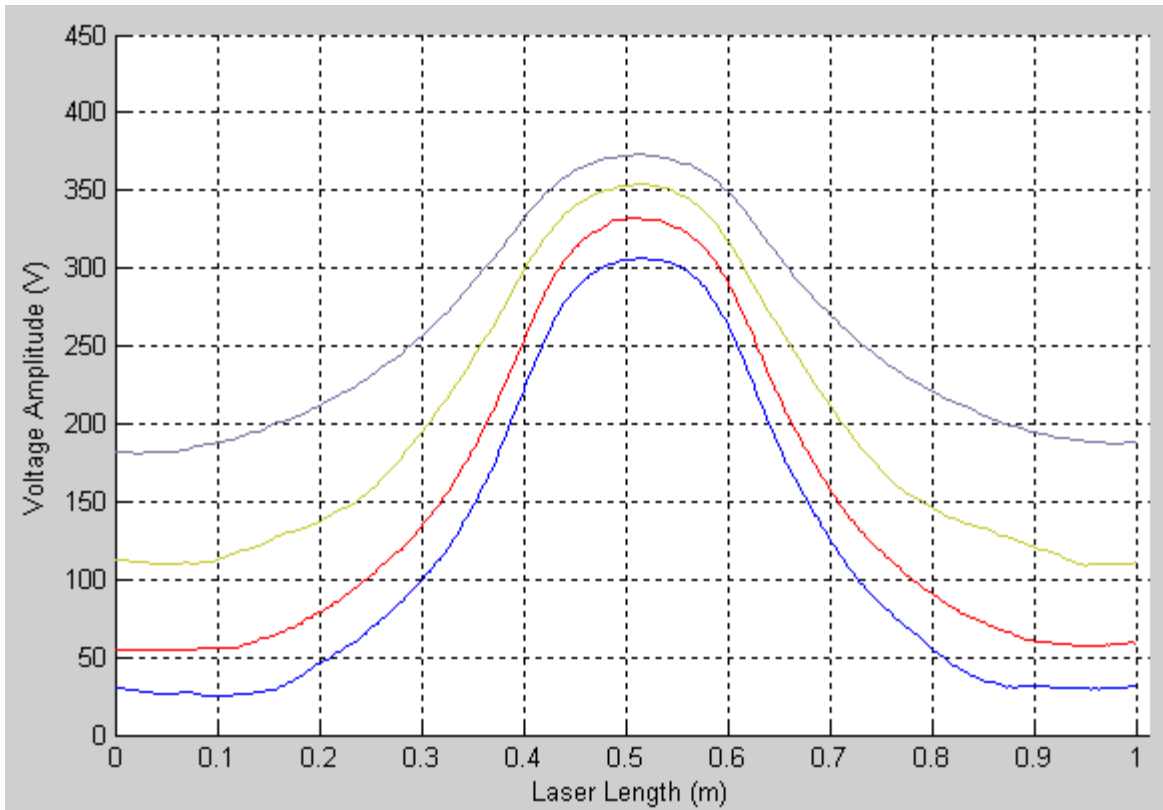
Figure 44: Voltage Distribution along the laser length at L_Y=7cm from the cermaic spacer / discharge area boundary.

The boundary conditions need to be investigated further, as the mirrors which are found in the X-dimension are good reflectors. However, in the Y-dimension the metal box which contains the laser is shielded and it is yet to be seen whether the inside of the casing is coated with any reflective material. Furthermore, it should be kept in mind that *Strohschein* in [2] claims that in wide channel devices the capacitive reactance of the high dielectric side walls formed by the ceramic spacers can make the TL properties insensitive to the laser discharge.

4.3 Validation of Computational Model

It is quite complicated to use a commercial solver such as Agilent's Advanced Design System (ADS) to model a TM field problem of such large proportions as a CO_2 slab laser. Furthermore, ANSOFT's HFSS is not an ideal candidate for model validation as our code requires an iterative scheme to solve for the circuit solution. We have used Prof. *Makarov's* FDTD code developed in his Computational Electromagnetics class for a voltage excitation of two parallel plates in an effort to validate our FDTD scheme. We note that this comparison is in the absence of laser discharge, and the intent is to show that the resulting electromagnetic fields are calculated properly. Figure 45 and Figure 46 show the results for a parallel plate simulation (metal boundary conditions), with the plates being 0.2mm apart, 1m in length, 0.25m in width, and excited by a 300Vrms voltage source.
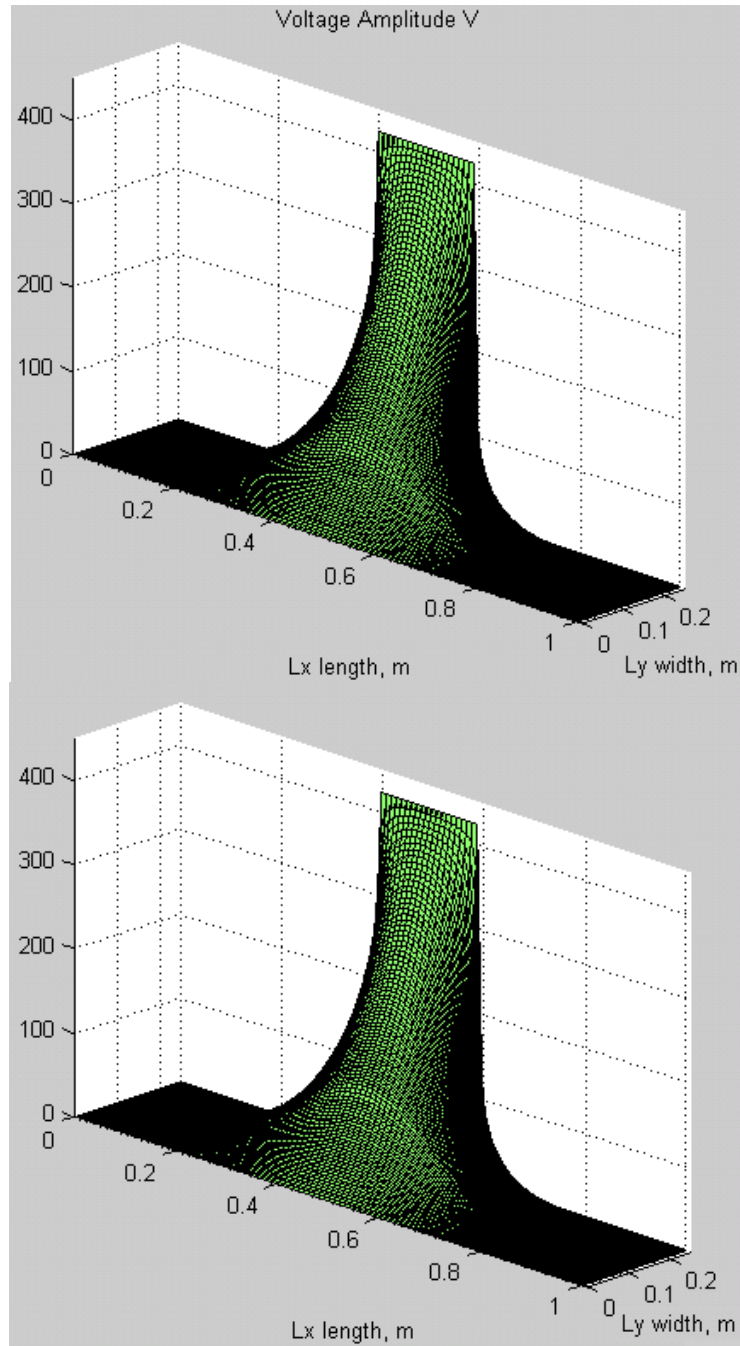
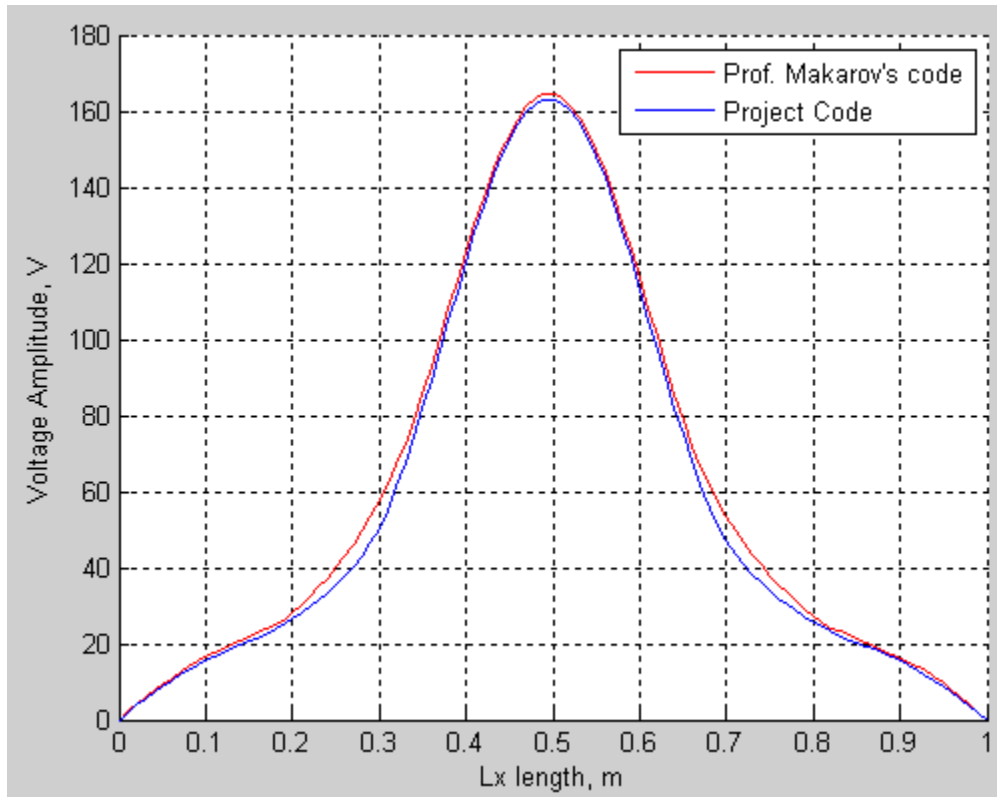Figure 45: Voltages at time t=T/4 for Prof. Makarov's code (top), and the project code (bottom).

Figure 46: Comparative Plot depicting the Voltage amplitude profile at Ly=0.5m cross section

The second approach that we used for model validation was to run simulation for lasers for which experimental data was available in literature. Two simulations were run using the same parameters as those presented in [2]. Figure 47 shows the results for a simulation which was run using parameters of f=82MHz, Vs=130Vrms, d=3.2mm, p=40torr, w=5cm, l=100cm and having two inductors of 15.5nH each. These parameters are the same as those reported in [2] to generate the plot shown in Figure 48. As can be seen there is a good level of agreement between the two plots. For CO_2 lasers higher pressures can lead to high discharge powers and hence inductor values will have to be changed to facilitate higher or lower power loading. Figure 49 shows results for a simulation which had the same parameters as Figure 47 except for a lower 20torr pressure and with two inductors of 29nH each. These parameters are the same as those for Figure 50. Again, as can be seen the agreement between the two figures is close.

Figure 47: Simulation results having the same parameters as [2] (see Figure 48).
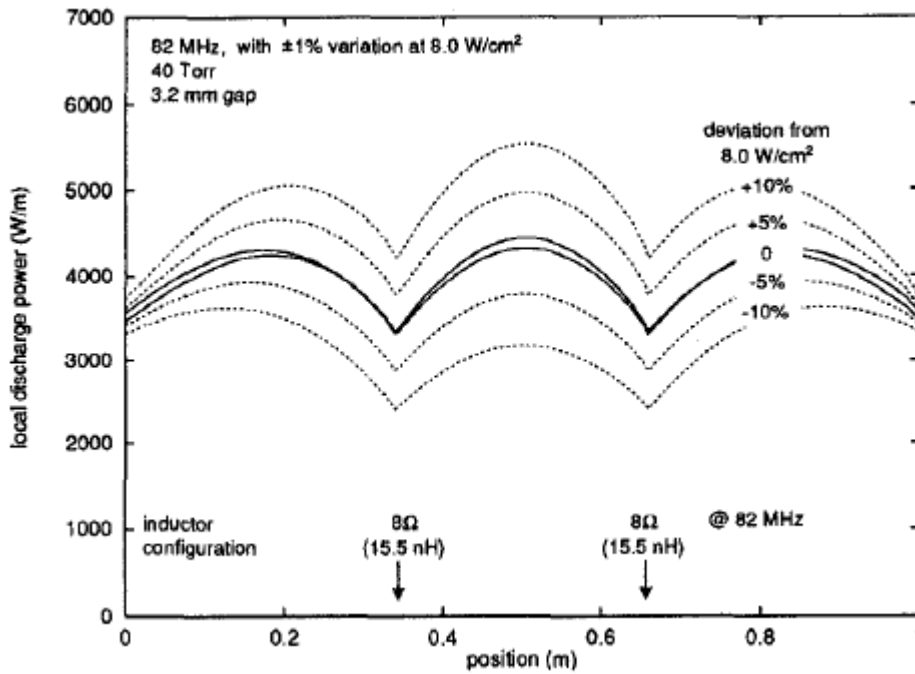
Figure 48: Results presented in [2] (with parameters of f =82MHz, Vs = 130Vrms, d = 3.2mm,
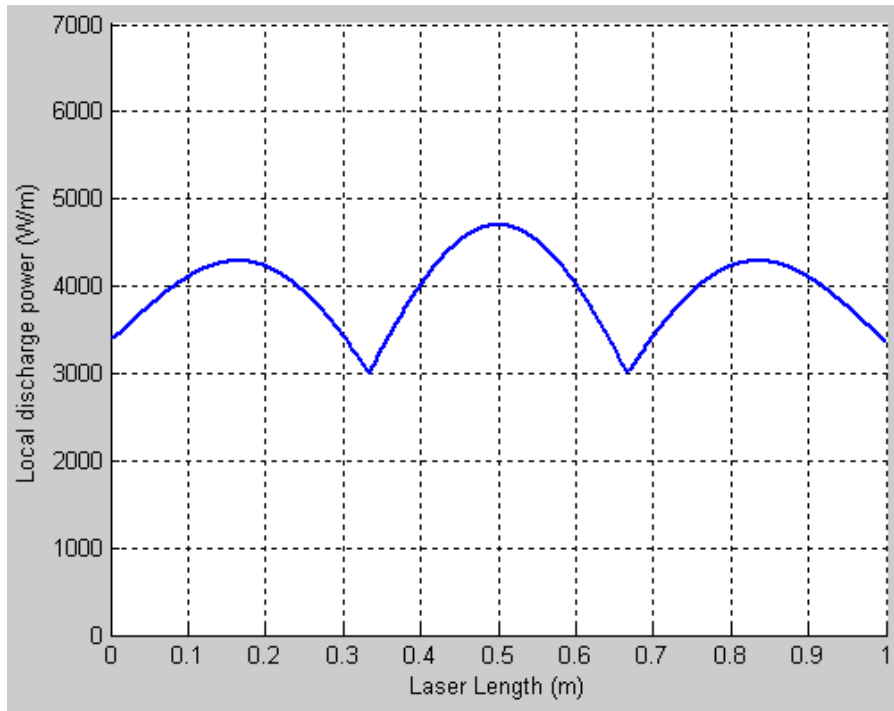
p=40torr, w = 5cm, l =100cm, two inductors of 15.5nH).

64
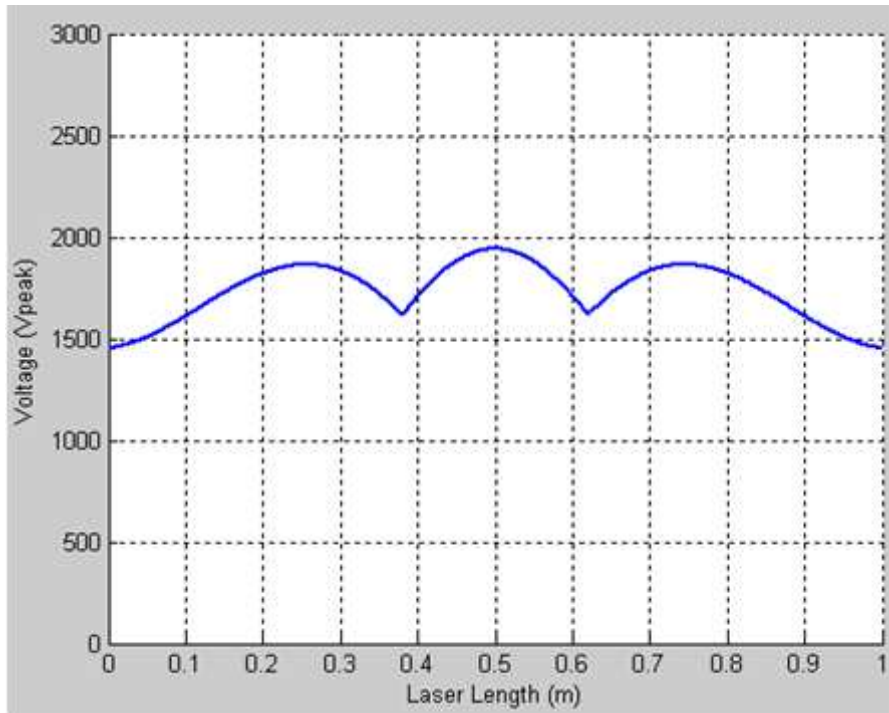
Figure 49: Simulation results having the same parameters as [2] (see Figure 48).
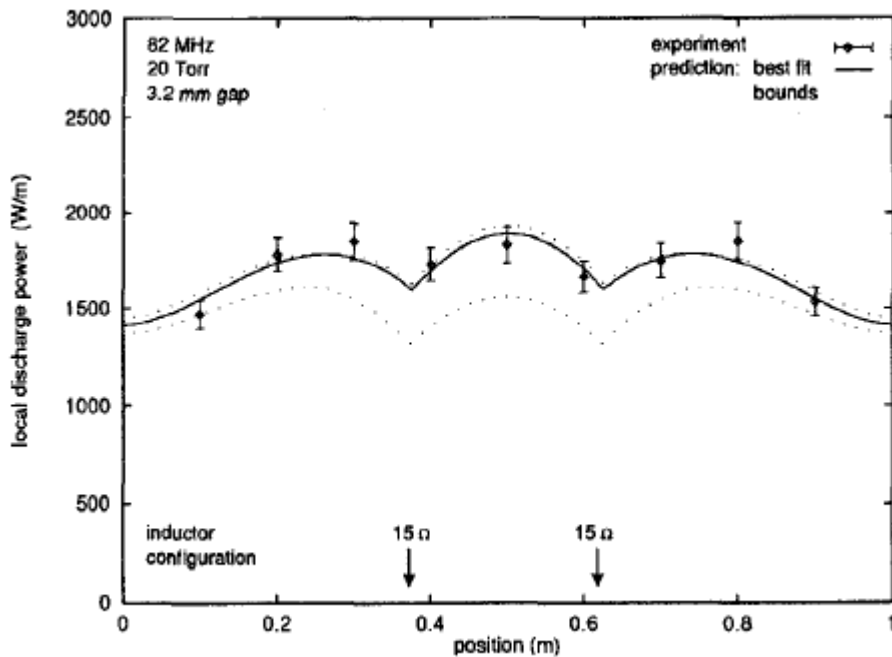
Figure 50: Results presented in [2] (based on parameters f =82MHz, Vs = 130Vrms, d = 3.2mm,

p=20torr, w = 5cm, l =100cm, and two inductors of 29nH).

We also compared our 2-D FDTD simulation results with those from [4], by running simulations for l=0.7m, w=0.1m, d=2mm, f=100MHz and using two 50nH termination inductors. The results can be seen in Figure 51, where as the data presented in [4] can be seen in Figure 52, and as expected fairly good agreement is seen between the two plots.
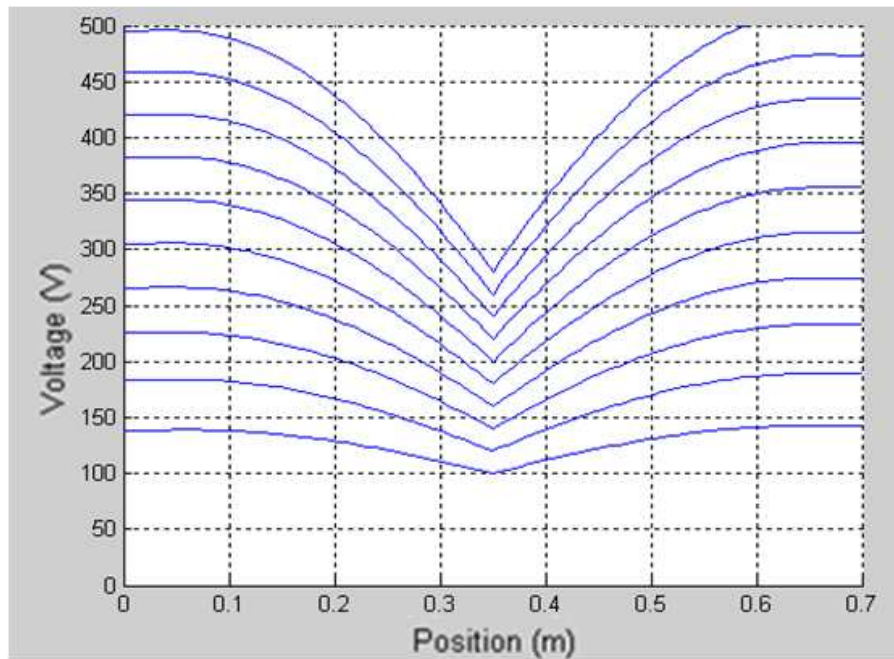
Figure 51: Simulation results with the same parameters as reported in [4] (see Figure 52).
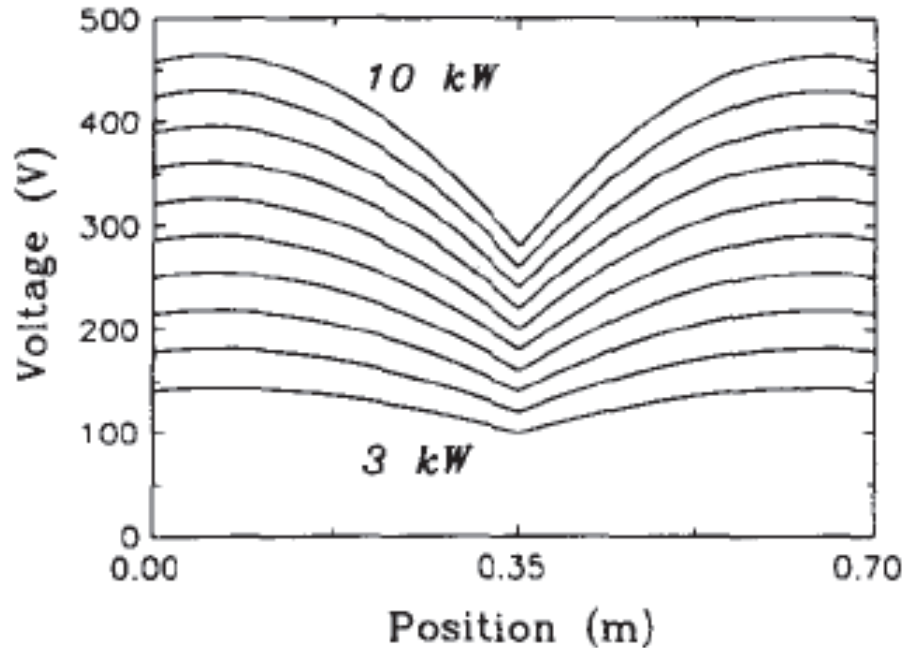
Figure 52: Results presented in [4] for l=0.7m, w=0.1m, d=2mm, f=100MHz and two 50nH inductors.

We also compared the results of both the 1-D and 2-D models by running simulations with varying aspect ratio geometries and using f=82MHz, Vs=110Vrms, d=3.2mm, p=20torr, w=5cm, l=100cm and two 20nH inductors. As expected, the comparison between the 1-D and 2-D model was very close for low aspect ratio of 0.05, but when increased to 0.2 the difference between the two outputs increased considerably. The simulation outputs shown in Figure 53 – 55 underscore this aspect. And it is the larger aspect ratios that are frequently of practical interested and having motivated the 2-D modeling efforts.
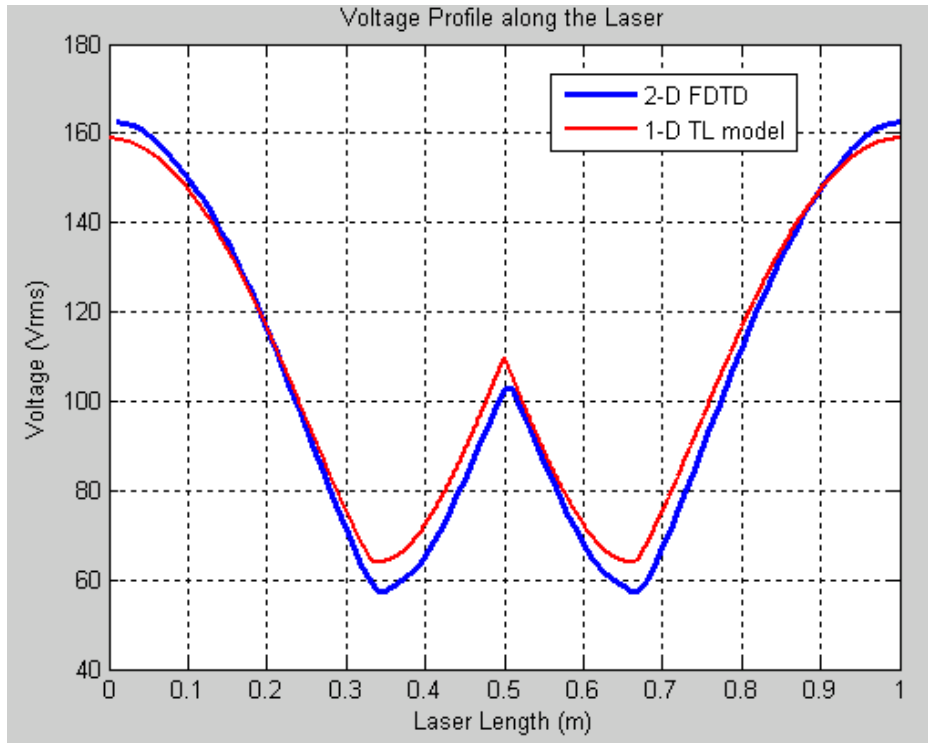
Figure 53: Comparison between 1-D and 2-D models for aspect ratio of 0.05
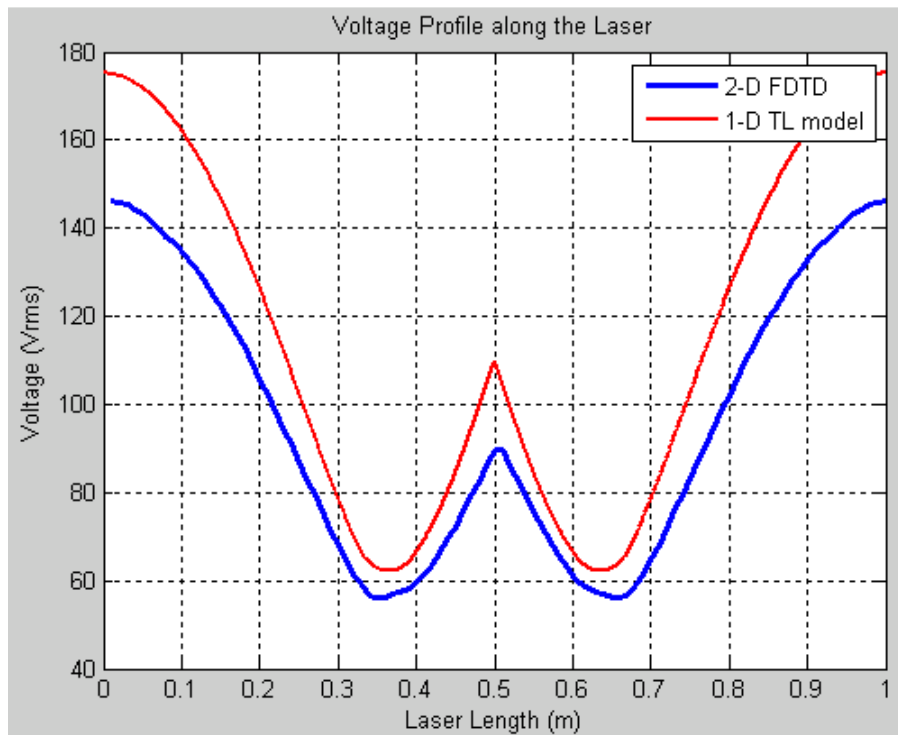
Figure 54: Comparison between 1-D and 2-D models for aspect ratio of 0.1
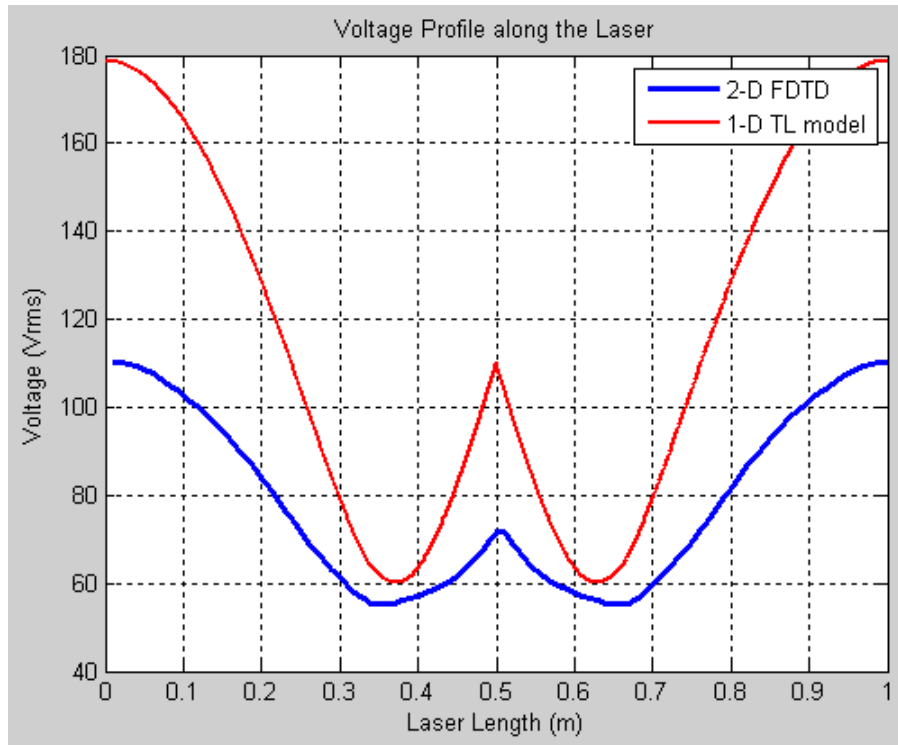
Figure 55: Comparison between 1-D and 2-D models for aspect ratio of 0.2

5 Conclusion

In this thesis comprehensive theoretical CO_2 laser models were developed and implemented in MATLAB. The scripts developed can be utilized for designing and investigating laser geometry and for analysis of laser efficiency, stability, power and heat analysis. The 1-D script is solved using the TL theory and is meant to be used for lower aspect ratio lasers, where as the 2-D script utilizes FDTD and can be used to model higher aspect ratio lasers.

6 Future Evolution and Enhancements

The scarcity of data in the open literature in regards to the CO_2 laser design is problematic, and requires a number of assumptions to be made before a laser geometry can be assumed for simulation. In addition, not having experimental access to an actual CO_2 laser along with equipment capable of measuring the voltage profile makes it difficult to optimize and enhance the models in an efficient and timely manner. Given these circumstances we had to use data available in [2], [4] and [6] for validation purposes.

In this thesis work attempts were made to take into account the effect of the ceramic spacers and the laser casing RF shielding on the discharge loading. The current set up of the 2-D code requires manual changing of the scripts, and moving the boundary conditions to simulate new laser geometries. This aspect of the code can be improved if a graphical interface can be adopted for geometry input and parameter selection.

A 3D model can also be useful, depending on the laser geometry.   Since we are interested in the voltage between the top and bottom slabs, modeling the TM mode should be adequate. However when we include the ceramic spacers in to our 2-D computational domain, we assume that ceramic spacers extend infinitely along the z-axis. Hence in this situation a 3-D model will be a better choice. The 3-D model will also help with 3-D thermal analysis. This addition of heat loss analysis should be a logical progression of our work as very often the laser power output levels are constrained by the type of cooling mechanism adopted and further the scripts already developed can be leveraged for adding thermal analysis functionality. A paper on longitudinal temperature variation along a gas laser geometry can be found in [21].

The models investigated in this work all used Vitruk's discharge model to predict the lumped impedance of the CO_2 laser discharge conditions. This model was constructed after experimental measurements were made for varying frequencies and pressures but for a specific

gas mixture. As CO_2 lasers use mixtures which have slightly varying constituents it will be beneficial to investigate their effect on results predicted by our models, and whether using a slightly different gas mixture can be ignored. It will also be interesting to research whether an analytical solution can be found to predict the laser discharge loading rather than using Vitruk's experimentally ascertained laser discharge model.

In the end we reiterate that it will be greatly helpful if any future work will model a laser for which physical measurements can be made. This will be a final and best validation of the models that have been investigated and improved in this work.

References

1. Wikipedia contributors. "Carbon dioxide laser." *Wikipedia, The Free Encyclopedia*. Wikipedia, The Free Encyclopedia, 11 Nov. 2010. Web. 27 Nov. 2010.

2. J. D. Strohschein, W. D. Bilida, H. J. J. Seguin, and C. E. Capjack, "Computational model of longitudinal discharge uniformity in RF-excited CO_2 slab lasers", *IEEE J. Quantum Electron.*, vol. 32, pp. 1289 - 1298, 1996.

3. K.M. Abramski, A.D. Colley, H. J. Baker, and D. R. Hall, "Power scaling of large-area transverse radio frequency discharge CO_2 lasers," *Appl. Phys. Lett.,* vol. 54, pp. 1833-1835, 1989.

4. A. Lapucci, F. Rossetti, M. Ciofini, and G. Orlando, "On the longitudinal voltage distribution in radio-frequency-discharged CO_2 lasers with large area electrodes," *IEEE J. Quantum Electron.,* vol. 31, pp. 1537-1541, 1995.

5. E. J. Plinski, J. S. Witkowski, and K. M. Abramski, "Algorithm of RF-excited slab-waveguide laser design," J. Phys. D: Appl Phys., vol. 33, pp 1823-1826, 2000.

6. Gerhard Spindler, "Two-Dimensional Computational Model of Discharge Uniformity in Radio-Frequency-Excited CO_2 Slab Lasers With High Aspect Ratio Electrodes," IEEE J. of Quantum Electronics, vol. 39, No. 2, 2003.

7. P. P. Vitruk, H. J. Baker, and D. R. Hall, "The characteristics and stability of high power transverse radio frequency discharges for waveguide CO_2 slab laser excitation," *J. Phys. D: Appl Phys.*, vol. 25, pp 1767-1776, 1992.

8. Wikipedia contributors. "Stimulated emission." *Wikipedia, The Free Encyclopedia*. Wikipedia, The Free Encyclopedia, 11 Nov. 2010. Web. 27 Nov. 2010.

9. Colin E. Webb, "Handbook of Laser Technology and Applications," Pg. 305. *IOP Publishing*, Philadelphia, 2004.

10. Marvin J. Weber, "Handbook of Lasers," Pg. 305. *CRC Press*, 2001.

11. Wikipedia contributors. "Solid-state laser." *Wikipedia, The Free Encyclopedia*. Wikipedia, The Free Encyclopedia, 29 Nov. 2010. Web. 29 Nov. 2010.

12. Rami Arieli, "Laser Adventure." Kansas State University Physics Education Research. http://web.phys.ksu.edu/vqm/laserweb/Ch-6/F6s2t1p1.htm

13. RP Photonics. "Quasi-continuous-wave Operation." Encyclopedia of laser physics and technology, 29 Nov 2010, Web 29 Nov. 2010.

14. Wikipedia contributors. "Dye laser." *Wikipedia, The Free Encyclopedia*. Wikipedia, The Free Encyclopedia, 29 Oct. 2010. Web. 1 Dec. 2010.

15. Frank Trager, "Springer Handbook of Lasers and Optics," Pg. 734. *Springer*, New York, 2007.

16. Wikipedia contributors. "Gas laser." *Wikipedia, The Free Encyclopedia*. Wikipedia, The Free Encyclopedia, 18 Oct. 2010. Web. 1 Dec. 2010.

17. Witteman, W.J.: The CO_2 laser, New York: Springer-Verlag, 1987.

18. Orazio Svelto*, "Principles of Lasers, 4th edition," Pg. 140. Springer*, New York, 1998.

19. H. J. Baker, "Direct measurement of the electrical impedance of narrow gap radio frequency gas discharges in the 100 MHz region," Meas. Sci. Technol., vol. 7, pp 1631-1635, 1996.

20. Adrian Muscat, "The Design of Low Gain, Wideband and Multi-band Antennas Employing Optimization Techniques," PhD Thesis submitted to *Queen Marry University of London*, 2001.

21. Rauf, A., B. Zhang, and J. Xin, "Longitudinal power distribution and corresponding temperature distribution in a RF waveguide CO2 laser," *PIERS Online*, Vol. 2, No. 6, 2006.

Appendix A – Lumped Components Incorporation in FDTD

The electric field update equation in FDTD is evaluated iteratively at every time step using the past values of E and H field, and a commonly used form is shown in Eq. (B.1). In FDTD, the past values of E and H field are denoted by E^n and $H^{n+1/2}$ respectively, and the next value of the E-field is represented by E^{n+1}.

$$E_Z^{n+1} = \left(\frac{1-\frac{\Delta t \sigma}{2\varepsilon}}{1+\frac{\Delta t \sigma}{2\varepsilon}}\right) E_Z^n + \left(\frac{\frac{\Delta t}{\varepsilon}}{1+\frac{\Delta t \sigma}{2\varepsilon}}\right) \left(\nabla \times H^{n+1/2}\right) \tag{B.1}$$

A lumped circuit component is easily incorporated into a FDTD simulation by altering the electric field update equation for the cell when the lumped component is added. The E-update equation is derived from Ampere's current law, Eq. (B.2) with Maxwell's correction, as the lumped component current enters the equation through the term J_L as shown below.

$$\nabla \times \underline{H} = \sigma \underline{E} + \varepsilon \frac{\partial E}{\partial t} + \underline{J_L} \tag{B.2}$$

Where,

$J_L = \frac{f(V_L)}{S}$, or a function of the Lumped component voltage V_L

S = Surface area of one face of the FDTD grid cell

ε = electric permittivity

σ = electric conduction

Next the space integral is applied to Eq. (B.2), and the resulting Eq. B.3 rearranged to give Eq. (B.4) which can be used to incorporate any kind of lumped component by substituting the component current as a function of the component voltage into Eq. (B.4).

$$\oint (\nabla \times \underline{H}) \cdot dS = \sigma \oint \underline{E} \, dS + \varepsilon \oint \frac{\partial E}{\partial t} dS + \underline{J_L} \tag{B.3}$$

Where for a TM mode,

$$\sigma \oint \underline{E} \, dS = \frac{\sigma}{2}(E_Z^{n+1} + E_Z^n)\Delta y \Delta x$$

$$\varepsilon \oint \frac{\partial E}{\partial t} dS = \frac{\varepsilon}{\Delta t}(E_Z^{n+1} - E_Z^n)\Delta y \Delta x$$

Eq. (B.4) can be rearranged to give Eq. (B.5), which is the E-update equation for any lumped component.

$$(\nabla \times H^{n+1/2})\Delta y \Delta z = E_Z^{n+1}\left(\frac{\sigma}{2} + \frac{\varepsilon}{\Delta t}\right) + E_Z^n\left(\frac{\sigma}{2} - \frac{\varepsilon}{\Delta t}\right) + f(V_Z) \tag{B.4}$$

$$E_Z^{n+1} = \left(\frac{1-\frac{\Delta t \sigma}{2\varepsilon}}{1+\frac{\Delta t \sigma}{2\varepsilon}}\right)E_Z^n + \left(\frac{\frac{\Delta t}{\varepsilon}}{1+\frac{\Delta t \sigma}{2\varepsilon}}\right)(\nabla \times H^{n+1/2}) - \left(\frac{\frac{\Delta t}{\varepsilon}}{1+\frac{\Delta t \sigma}{2\varepsilon}}\right)\frac{f(V_Z)}{\Delta y \Delta x} \tag{B.5}$$

Impedance Voltage Source

A current source can be incorporated into the model by using the voltage Eq. (B.6).

$$V_Z = V_{source} - I_{source}.R_{source} \tag{B.6}$$

Which when solved for I_source by using the FDTD notation becomes Eq. (B.7).

$$I_{source} = \frac{V_Z - V_{source}}{R_{source}} = \frac{\frac{\Delta z}{2}(E_Z^{n+1} + E_Z^n) - V_{source}}{R_{source}} \tag{B.7}$$

And finally on substituting I_source into Eq. (B.5) we obtain the E update equation for an impedance soft source shown in Eq. (B.8).

$$E_Z^{n+1} = \left(\frac{1-\frac{\Delta t \sigma}{2\varepsilon}-C}{1+\frac{\Delta t \sigma}{2\varepsilon}+C}\right)E_Z^n + \left(\frac{\frac{\Delta t}{\varepsilon}}{1+\frac{\Delta t \sigma}{2\varepsilon}+C}\right)(\nabla \times H^{n+\frac{1}{2}}) - \left(\frac{\frac{\Delta t}{\varepsilon}}{1+\frac{\Delta t \sigma}{2\varepsilon}+C}\right)\frac{V_{source}}{R_{source}\Delta y \Delta x} \tag{B.8}$$

Where,

$$C = \frac{\Delta t \Delta z}{2\varepsilon R_{source}\Delta x \Delta y}$$

Lumped Resistors

For a resistor the current equation becomes Eq. (B.9), which when substituted in to Eq. (B.5) gives Eq. (B.10) which is further simplified into the E-update Eq. (B.11).

$$I_{resistor} = \frac{V_Z}{R} = \frac{E_Z \Delta z}{R} = \frac{(E_Z^{n+1} + E_Z^n)\Delta z}{2R} \tag{B.9}$$

$$E_Z^{n+1} = \left(\frac{1 - \frac{\Delta t \sigma}{2\varepsilon}}{1 + \frac{\Delta t \sigma}{2\varepsilon}}\right)E_Z^n + \left(\frac{\frac{\Delta t}{\varepsilon}}{1 + \frac{\Delta t \sigma}{2\varepsilon}}\right)(\nabla \times H^{n+1/2}) - \left(\frac{\frac{\Delta t}{\varepsilon}}{1 + \frac{\Delta t \sigma}{2\varepsilon}}\right)\frac{\Delta z(E_Z^{n+1} + E_Z^n)}{2R \Delta y \Delta x} \tag{B.10}$$

$$E_Z^{n+1} = \left(\frac{1 - \frac{\Delta t \sigma}{2\varepsilon} - \frac{\Delta t \Delta z}{2\varepsilon R \Delta x \Delta y}}{1 + \frac{\Delta t \sigma}{2\varepsilon} + \frac{\Delta t \Delta z}{2\varepsilon R \Delta x \Delta y}}\right)E_Z^n + \left(\frac{\frac{\Delta t}{\varepsilon}}{1 + \frac{\Delta t \sigma}{2\varepsilon} + \frac{\Delta t \Delta z}{2\varepsilon R \Delta x \Delta y}}\right)\left(\nabla \times H^{n+\frac{1}{2}}\right) \tag{B.11}$$

Lumped Inductors

The first order differential equation for a lumped inductor is given by Eq. (B.12) or in a Finite Difference form in Eq. (B.13).

$$\frac{dI_{inductor}}{dt} = \frac{(V)}{L} \tag{B.12}$$

$$I^{n+\frac{1}{2}} = I^{n-\frac{1}{2}} + \frac{\Delta t V^n}{L} \tag{B.13}$$

Further considering that the initial inductor current is zero the inductor current is given by Eq. (B.14).

$$I_{inductor} = \frac{\Delta t}{L} \sum_{m=1}^n \frac{V^m}{L} = \frac{\Delta t \Delta z}{L} \sum_{m=1}^n \frac{E^m}{L} \tag{B.14}$$

Where,

$$J_{inductor} = \frac{I_{inductor}}{\Delta x \Delta y} \tag{B.15}$$

Since the inductor current is a energy storage device the current through it does not change instantaneously and hence that is why the inductor current equation does not contain the E_{n+1}

term and hence adding a inductor to the E-update equation is even simpler as it does not

required any further simplification, the E-update equation for an inductor is given in Eq. (B.16).

$$E_Z^{n+1} = \left(\frac{1-\frac{\Delta t\sigma}{2\varepsilon}}{1+\frac{\Delta t\sigma}{2\varepsilon}}\right)E_Z^n + \left(\frac{\frac{\Delta t}{\varepsilon}}{1+\frac{\Delta t\sigma}{2\varepsilon}}\right)\left(\nabla \times H^{n+1/2}\right) - \left(\frac{\frac{\Delta t}{\varepsilon}}{1+\frac{\Delta t\sigma}{2\varepsilon}}\right)\frac{\Delta t\Delta x}{L}\sum_{m=1}^{n}\frac{E^m}{L} \qquad (B.16)$$